12-2013

APPLICATION OF IMAGE PROCESSING AND FINITE ELEMENT ANALYSIS IN MODELING CHLORIDE DIFFUSION IN CONCRETE

Arash Razmjoo
Clemson University, arazmjo@g.clemson.edu

APPLICATION OF IMAGE PROCESSING AND FINITE ELEMENT ANALYSIS IN MODELING CHLORIDE DIFFUSION IN CONCRETE

A Dissertation
Presented to
the Graduate School of
Clemson University

In Partial Fulfillment
of the Requirements for the Degree
Doctor of Philosophy
Civil Engineering

---

by
Arash Razmjoo
December 2013

Accepted by:
Dr. Amir Poursaee, Committee Chair
Dr. Prasad Rao Rangaraju
Dr. Bradley Putman
Dr. Firat Testik

ABSTRACT

Utilizing numerical simulation models to predict the long-term mechanical and transport behavior of concrete structures is becoming increasingly popular. The majority of these models have been developed using laboratory test data that consider concrete as a homogeneous material with spherical aggregates. These models could not be a represented of real concrete because it has no primitive shaped aggregate besides that the porosity size and distribution varies from point to point.

In this study a novel method for more accurate prediction of the chloride diffusion in concrete was developed. A general framework of the quantitative computed tomography (QCT) and finite element analysis was used to construct 3D images of concrete cylinders. A computer code was developed using Matlab to analyze images and to measure the amount and distribution of coarse aggregates and voids in the concrete cylinders. The rapid performance and independency from personnel, as well as the capability of inspecting the internal structure and possible damages within the cylinders, make this method very applicable for quality control and quality assurance applications as well as for forensic investigations.

During this study, it was realized that the shape and distribution of aggregates as well as Interfacial Transition Zones (ITZs) have significant impact on the chloride diffusion into the concrete. Therefore, it was imperative to construct a predictive model which was

closer to reality, considering the distribution of aggregate particles (coarse and fine), voids, and ITZs (around both coarse and fine aggregates). Thus, a numerical method for the prediction of the chloride penetration into concrete was developed using a scanned copy of the concrete internal structure.

The results obtained from this study showed that, QCT along with image analysis techniques used to study the air void content and distribution as well as coarse aggregate content in concrete in 3D had a good agreement with the microscopic analysis. The major advantage of QCT technique is much short time required for analysis with the QCT method compared to that with the conventional microscopic studies. The result from the chloride diffusion in concrete showed that chloride concentration gradient when ITZ is considered around aggregates is much higher compared to that in concrete without considering the ITZ. The positions and shapes of the coarse aggregates can also affect the diffusion process and the chloride ion diffusivity. The experimental and simulation results indicated that closer aggregates to the steel bar can increase the rate of the chloride diffusion as well as the rate of corrosion.

DEDICATION

I dedicate this dissertation to my loving parents who brought me up with care and kindness and have always supported me and my work. I also dedicate this to my dearest caring wife, Lida for her patience and sacrifice during 8 years studying two PhDs, without her continuous support and persistent help, these process would not have been possible. I also dedicate this to my wonderful daughter Ellena.

ACKNOWLEDGMENTS

I would like to express my greatest appreciation to all my PhD committee members for the assistance they provided at all levels of this research project. My special gratitude goes to my PhD advisor Dr. Amir Poursaee for his innumerable hours of reflecting, pondering, encouraging, and guiding throughout the entire duration of my work. Without his continuous guidance and persistent help, this dissertation would not have been possible.

I appreciate the feedback I have received from Dr. Prasad Rangaraju, Dr. Bradley Putman and Dr. Firat Testik.

I would also like to express my deepest gratitude to Professor Mohammad Parnianpour for his continuous encouragement.

I would like to acknowledge the support provided by Clemson University's faculty and staff. I would also like to thank Mr. Danny Metz and his team from Civil Engineering, for maintaining the equipment in the lab and helping me with operating the equipment. I also thank Dr. Punith Shivaprasad, Mrs. Cindy McMahan and Dr. Shifeng Wang, from ARTS center.

I would like to thank my friends, fellow graduate students and my lab mates, Faz Sadeghi, Matthew Adamson, Masoud Shirazi, Farzam Safarzadeh, Shubhada Gadkar and Trent Dellinger.

I recognize that this research would not have been possible without the financial assistance of the Department of Civil Engineering at Clemson University through research assistantship. I express my gratitude to them.

TABLE OF CONTENTS

LIST OF TABLES

LIST OF FIGURES

CHAPTER 1: INTRODUCTION

Considering the high costs for annual rehabilitation and restoration of concrete infrastructure; predicting the response of a concrete structure to real situations is a major concern for owners and investigators. This prediction can provide a preferential plan for reducing the rehabilitation cost and time, which ultimately increase the reliability and durability of such a structure. Therefore, predicting the service life of concrete structures is a major concern toward a sustainable design. The behavior of concrete infrastructure is drastically affected by the percentage of aggregates and air voids in the mixture and their distribution within the concrete. Measuring these two components is used for quality control purposes both in under construction and older buildings. However, time consumption and personnel dependency of this measurement makes it difficult to conduct accurately. In this study the conventional Computer-Tomography Scanning system (CT-Scan) was used to construct 3D images of concrete cylinders. A computer code was developed using Matlab to analyze images and to measure the amount and distribution of coarse aggregates and voids in the cylinders. The rapid performance and independency from personnel, as well as the capability of inspecting the internal structure and possible damages within the cylinders, make this method very attractive for quality control and quality assurance applications as well as for forensic investigations.

One other application of such realistic modeling approach is more accurate prediction of the service life and the response of a concrete body to a stimulus element, using finite element and

numerical analyses. One example is chloride diffusion into the steel reinforced concrete structures which causes corrosion in such a structure.

Corrosion of the reinforcing steel bars, resulting from chloride ions diffusion has significant impact on the durability of steel reinforced concrete structures. Concrete mixture proportions and its constituents greatly influence the chloride diffusion and consequently the corrosion of the steel bars. Thus to study the effect of chloride diffusion into the concretes it is necessary to build a more accurate model which is closer to reality considering the distribution of aggregate particles (coarse and fine), voids, and Interfacial Transition Zones (ITZs). In this study, a numerical method for the prediction of the chloride penetration into concrete was developed using a realistic concrete internal structure. To represent the concrete model as realistically as possible, a two dimensional simulation for the distribution of fine aggregates, coarse aggregates, ITZs and voids in concrete was developed.

The main objectives of this research were:

1. Precisely calculating the amount and 3D distribution of coarse aggregates and voids in the concrete by utilizing the image processing methods.
2. Developing a novel model for more accurate prediction of the chloride diffusion into concrete using the general framework of the image processing and finite element analysis.

The objectives of this study were accomplished through the completion of the steps described below:

Step I

- QCT imaging
  - Sample preparation
  - Performing CT scan and collecting data
- Image processing
  - Surrounding elimination
  - Image enhancement and filtering

Step II

- Void detection
  - Measurement and distribution
- Coarse aggregates discrimination
  - Measurement and distribution
- 3-D model
  - Inside viewing
  - Defect detection

Step III

- Meshing
  - Nodes
  - Elements
  - Material properties
- Finite element modeling
  - Material model (linear elastic-perfectly plastic)

Boundary condition

Step IV

2-D Image processing

Air void detection

Coarse aggregates detection

Fine aggregate detection

Finite element modeling

Nodes and elements

ITZ around coarse and fine aggregates

Material properties

Finite element post-processing

Chloride concentration pattern

Corrosion initiation time

CHAPTER 2: LITERATURE REVIEW

2.1. Basic concepts in digital image processing

Images are produced by a variety of physical devices, including still and video cameras, scanners, X-ray devices, electron microscopes, radar, and ultrasound. They can be used for a variety of purposes, including: entertainment, medical imaging, business and industry, military, civil, security, and scientific analyses, as illustrated in Figure 2.1.1

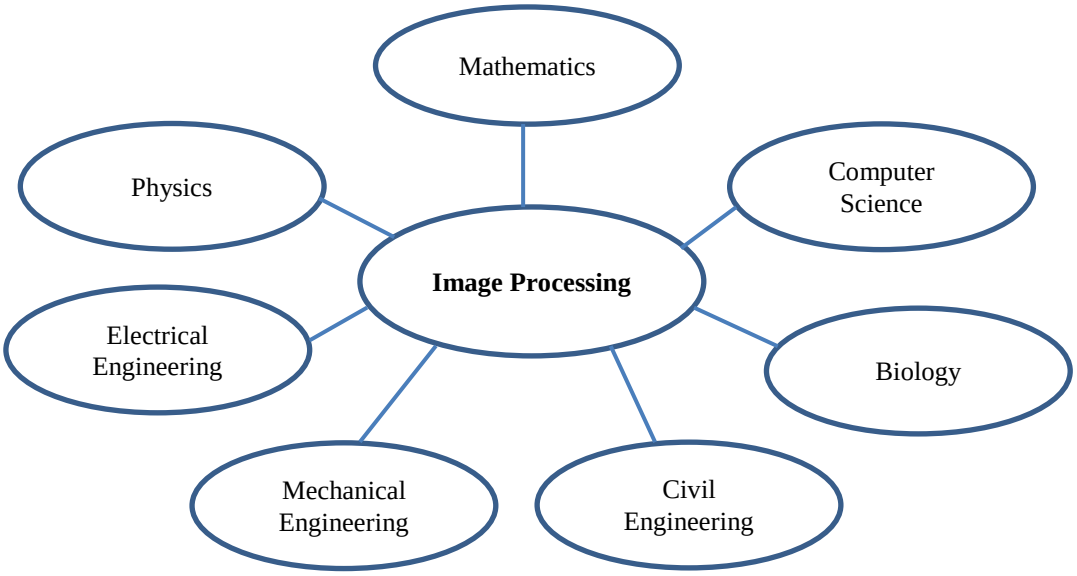

Figure. 2.1.1 Sciences related to image processing

This interest in digital image processing originates in the improvement in the quality of pictorial information available for human interpretation and the processing of much more complex image for autonomous machine perception (Shih 2009). A digital image is a collection of numbers representative of a two-dimensional image that has been discretized in both spatial coordinates and brightness (intensity). The image is divided into small regions called picture elements, or

pixels (see Figure 2.1.2). Image digitization is a process that converts a pictorial form to numerical data. Digital image processing is the computer-based analysis and modification of digital images to extract desired information.

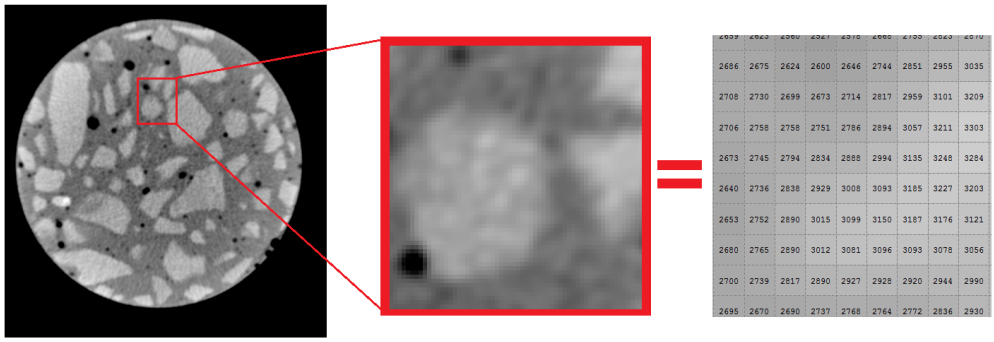

Figure. 2.1.2 An image of concrete together with its pixel numbers representation

2.2. Application of digital image processing in civil engineering

Many techniques of digital image processing were developed in the 1960s for satellite imagery and medical imaging. However, due to the high cost of digital image processing, it was not widely applied to other disciplines and industries until the 1990s when low-cost personal computers and digital cameras became available. Since then, digital image processing techniques have been adapted to many civil engineering applications as well. The capability to automatically identify shapes, objects and materials from the image content through direct (content-based) and indirect methodologies enable the development of civil engineering tools. These tools utilize image data to assist in the design, construction and maintenance of construction projects. Motion segmentation to detect moving vehicles (Koller et al. 1993) and edge detection techniques to detect the type and amount of surface cracks in pavements (Abdel-Qader et al. 2003), using the image color and intensity to assess fire-damaged mortar (Lin et al. 2004), image analysis to

determine the strain distribution in geosynthetic tensile testing (Aydilek et al. 2003), evaluating the fatigue of asphalt mixes (Hartman et al. 2004), using image velocimetry for flow diagnostics in fluid modeling (Muste et al. 2004), performing multi-resolution pattern classification of steel bridge coating (Chen et al. 2002), and using computed tomography (CT-Scan) to detect the internal structure of asphalt concrete (Aydilek et al. 2002), the shapes of aggregates (Garboczi 2002) and evaluate microstructure of mortars (Lanzón et al. 2012), are some of the examples.

2.3. Computed Tomography (CT)-scan

The word "tomography" is derived from the Greek tomos (slice) and graphein (to write). The objective of CT is obtaining a three-dimensional image of the internals of an object from a large series of two-dimensional X-ray images taken through that object. CT was developed by a British engineer Sir Godfrey Hounsfield and Dr. Alan Cormack in the early 1970s (Rangayyan 2005). CT scans, allow us to look inside a body non-invasively. Advances in computer technology have vastly improved CT scanners. These improvements have led to faster imaging and higher-resolution images. Since then, computers have become integral components of modern imaging systems and performing a variety of tasks from data acquisition and image generation to image display and analysis are based on this ability.

2.4. How does a CT-scan work?

X-ray radiography measurements are based on the concept that as X-rays pass through a material, some of its intensity is attenuated by the material while a portion of the X-ray's intensity pass through the material and is captured using an X-ray detector. The amount of the X-

ray attenuated is related to the density of the material that the X-ray is passing through. This concept is schematically shown in Figure 2.4.1.

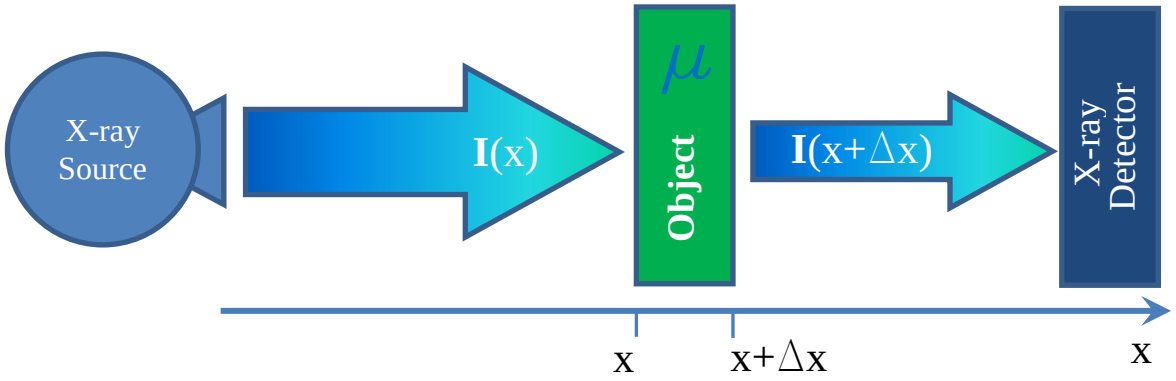

Figure. 2.4.1. X-ray attenuation mathematical model while running through a homogeneous object with constant attenuation μ

Within this simple model the total attenuation of a monochromatic X-ray beam can be calculated. The radiation intensity, which is proportional to the number of photons, after passing a distance Δx through an object, is determined by:

$$I(x + \Delta x) = I(x) - \mu(x)I(x)\Delta x. \qquad \text{(eq. 2.4.1)}$$

By simple reordering of eq. 2.4.1, the eq. 2.4.2 can be obtained:

$$\frac{I(x + \Delta x) - I(x)}{\Delta x} = -\mu(x)I(x) \qquad \text{(eq. 2.4.2)}$$

Taking the limit of eq. 2.4.2 as Δx approaches zero leads to the differential quotient:

$$\lim_{\Delta x \to 0} \frac{\mathrm{I}(x + \Delta x) - \mathrm{I}(x)}{\Delta x} = \frac{dI}{dx} = -\mu(x)\mathrm{I}(x) \qquad \text{(eq. 2.4.3)}$$

In a first step, the medium is assumed to be homogeneous, i.e., in eq. 2.4.3 the object can be described by a single attenuation constant $\mu(x) \equiv \mu$ along the entire length of penetration. This leads to an ordinary linear and homogeneous first order differential equation with constant coefficients. The solution is obtained by separation of variables. Consider the right-hand side of eq. 2.4.3, which can be separated to

$$\frac{dI}{I(x)} = -\mu(x)\,dx \qquad \text{(eq. 2.4.4)}$$

Integration of both sides of eq. 2.4.4 gives:

$$\int \frac{dI}{I(x)} = -\mu \int dx \Rightarrow \ln|I| = -\mu x + C \qquad \text{(eq. 2.4.5)}$$

Subsequent exponentiation leads to

$$I(x) = e^{-\mu x + C} \qquad \text{(eq. 2.4.6)}$$

With the initial condition $I(0) = I_0$, the special solution of the differential equation eq. 2.4.3 gives the Beer's law of attenuation:

$$I(x) = I_0 e^{-\mu x} \qquad \text{(eq. 2.4.7)}$$

If the attenuation coefficient varies discontinuously, as schematically illustrated in Figure 2.4.2, the intensity reduction while running through the object can be estimated without solving a differential equation.

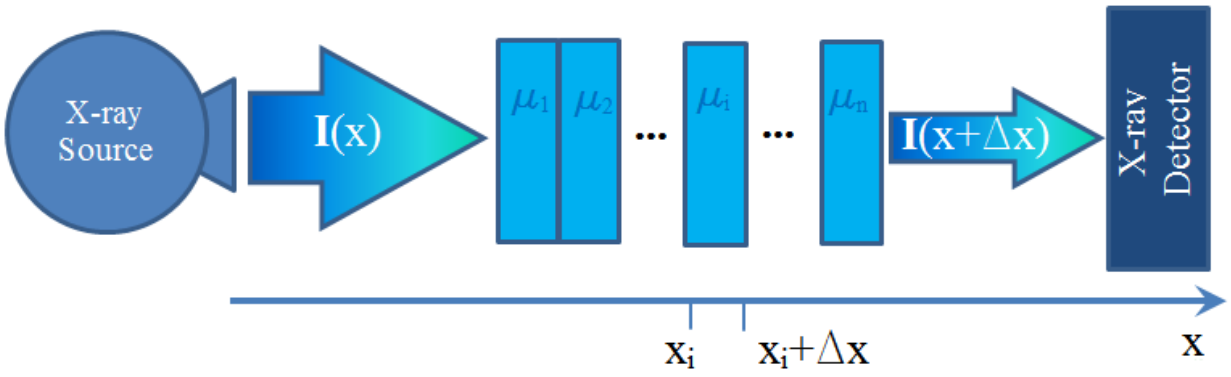

Figure. 2.4.2. X-ray attenuation mathematical model while running through series of objects.

In this model, when an x-ray with intensity I_i passes through the object, i+1 with thickness Δx, it will attenuate to the intensity of I_{i+1} and attenuation coefficient, μ_{i+1} can be obtained.

$$I_{i+1} = I_i - \mu_{i+1} I_i \Delta x = I_i (1 - \mu_{i+1} \Delta x) \qquad \text{(eq. 2.4.8)}$$

Consequently, the total attenuation is a series of products:

$$I_n = I_0 (1 - \mu_1 \Delta x)(1 - \mu_2 \Delta x)...(1 - \mu_i \Delta x)...(1 - \mu_n \Delta x) \qquad \text{(eq. 2.4.9)}$$

If the discretization of the object is very fine, i.e., Δx is chosen to be small, the factor terms in parentheses can be interpreted as the Taylor expansion of the exponential function. With

$$e^{-\varepsilon} \approx 1-\varepsilon \qquad \text{(eq. 2.4.10)}$$

For small ε, the approximation can be obtained.

$$I_n \approx I_0 e^{-\mu_1 \Delta x} e^{-\mu_2 \Delta x} ... e^{-\mu_i \Delta x} ... e^{-\mu_n \Delta x} \qquad \text{(eq. 2.4.11)}$$

By taking the limit $\varepsilon \to 0$ the exact equation can be obtained

$$I_n = I_0 e^{-\sum_{i=1}^{n} \mu_i \Delta x} \to I_0 e^{-\int \mu(x) dx} \qquad \text{(eq. 2.4.12)}$$

Based on Beers law, high values of the attenuation coefficient, μ, are due to a high density or high atomic number of the object.

Unlike an X-ray machine which sends just one radiation beam, a CT scanner emits a series of X-ray beams through the object body and projects all of the obtained information into a two dimensional detecting screen. The final picture is far more detailed than an image obtained from one X-ray beam. The data obtained from the CT scan, are transmitted to a computer, which builds up a 3-D cross-sectional picture of the part of the body under investigation and then displayed on the screen. The accuracy and speed of CT scan may be improved with the application of spiral CT. In this system, the X-ray beam takes a spiral path during the scanning and it gathers continuous data with no gaps between images. In 3-D digital radiology, the

attenuation coefficient in each portion of the volume of interest is expressed by a number called the CT Number.

CT numbers correlate to gray levels, or gray shades, when the volumetric dataset is rendered into images. It is important to note that the output of the sensors must be processed by reconstruction algorithms whose objective is to transform the sensed data into meaningful cross-sectional images. Sensor strips mounted in a ring configuration are used in medical and industrial imaging to obtain cross-sectional or slice images of 3-D objects, as Figure 2.4.3 shows.

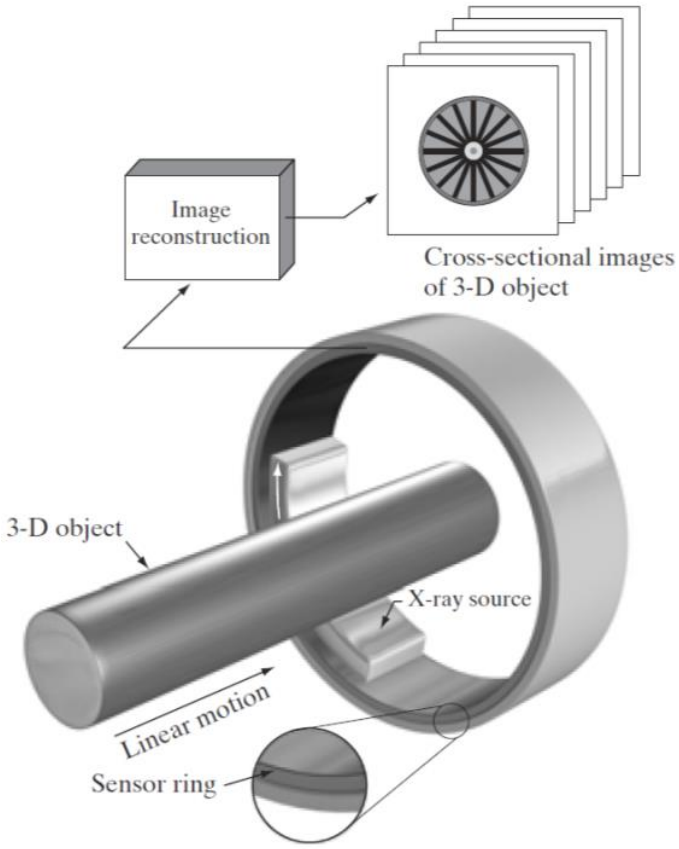

Figure. 2.4.3. Composition of table feeding with rotation of X-ray source and detectors makes a spiral CT scanning (Gonzalez et al. 2009)

A rotating X-ray source provides radiation and the portion of the sensors opposite the source collect the X-ray energy that pass through the object. The output of most sensors is a continuous voltage waveform whose amplitude and spatial behavior are related to the physical phenomenon being sensed (Gonzalez et al. 2009). A Quantitative (Q) CT device, as the name shows, by using the abovementioned equations, converts continuous sensed data into digital form (quantization). Figure 2.4.4 illustrates a concrete cylinder sample along with its processed QCT images indicating aggregates and air voids inside it which can be calculated non-invasively.

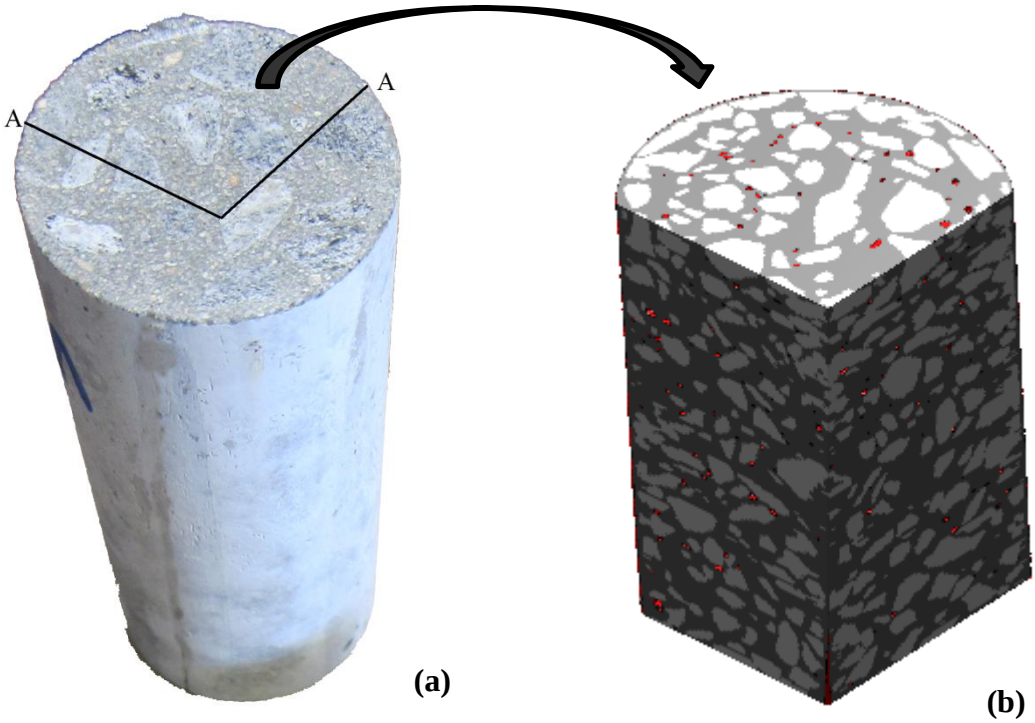

Figure. 2.4.4 (a) concrete cylinder, (b) aggregates (light gray), cement matrix (dark gray) and air voids (red spots) inside processed QCT model.

2.5. Image processing in concrete materials

As mentioned before, CT scan and image processing have been used to study concrete materials. Porosity profile of pervious concrete was obtained from processing of CT scanned images

(Manahiloh et al. 2012). This study was restricted to porosity as a quantifying parameter; however, the images and their characterization for identifying the shape, size, and distribution of particles were not considered. Lanzon and his colleagues examined the porosities of mortar by using micro CT (μ-CT) technique (Lanzón et al. 2012). In this study, the mortar microstructure was studied in terms of porosity and the equivalent diameter of the pores. The nature of the mortars permits precise segmentation as air is clearly differentiated from the solid components due to its low density. However, it should be mentioned that application of the μ-CT technique is limited by the size of the specimen otherwise many visible defects on the images (artifacts) is created which makes them ineffective. Therefore, μ-CT is not applicable for concrete samples because the small size of the sample cannot be considered a good representative of real concrete structure. A 3-D multi-scale model of mechanical properties of cement-based materials was suggested by Bernard and his colleagues (Bernard et al. 2008). This model takes into account the eventual changes in the micro-structure. Two numerical tools are combined including chemical model of cement based materials and finite element model (FEM) to predict mechanical behavior and effect of leaching. However, this research only considered a 5 millimeter cube of mortar consists of small sand particles in cement paste in meso-scale to determine its mechanical behavior and Young's modulus. In their FEM, fine aggregates were considered as spheres regardless of their real non primitive shape. In another study, damage mechanism of concrete under hydrostatic and triaxial loadings was investigated using CT technique (Poinard et al. 2012). The study performed by applying high-pressure triaxial load followed by CT scan. Scanned images prior to the initial loading and after each cycle were compared. Image analyses indicated that under high hydrostatic loading, significant damage was visible in cement paste at the mesoscopic scale. At the lower pressure, shear loading created a

localized failure mechanism characterized by sliding on an inclined plane, whereas at the higher pressure, the strain and damage mode were much more homogeneous with failure localization after unloading. In this research, it was found that the damage mechanism on concretes was not greatly under the influence of the shape of aggregates. However, this observation is opposite of what Garboczi found in his research (Garboczi 2002). The main reason hypothesized by Garboczi is that aggregates with different shapes generate different ITZ specification which is directly related to damages in concrete.

It should be emphasized that in all of the abovementioned studies, images were manually processed. The disadvantages of manual image processing which have been mentioned by Russ (Russ 2011) can be summarized as:

- Manual adjustment of thresholds to produce a result that is considered to be correct based on visual inspection by a human operator might cause several errors and should be avoided as much as possible,
- It is a time consuming process,
- Different results are likely to be obtained at different times, by different people,
- Manual thresholding errors are probably responsible for more problems in subsequent image analysis than any other cause.

2.5. Interfacial transition zone

In the neighborhood of an aggregate in concrete the microstructure of cement paste is different from that part of cement paste which encapsulates no aggregates (Garboczi et al. 1991; Scrivener et al. 1996). This area is called Interfacial Transition Zone (ITZ). The idea of an ITZ in concrete

was developed initially by Farran (Farran 1956). When the cement grains meeting the surface of the aggregate, due to the packing constraints imposed by the aggregate's wall, a region appears near the aggregate surface which has higher porosity than another places of paste (Ollivier et al. 1995; Zheng et al. 2005). Despite the difference of ITZ from a bulk paste, it is not a discrete zone but a region with gradually changing microstructure (Scrivener et al. 2004). The first experimental technique for analysis of the ITZ was developed by Scrivener and his colleagues. In their study, they found that porosity concentration near the interface is higher due to poorly packing of un-hydrated cement along the interface. They argued that poorly packed cement particles along the interface leads to localized high water to cement ratio, causing an increase in capillary porosity and the concentration of hollow shelled hydration grains (Scrivener et al. 1986). In a study by Ping and his colleagues, the electrical conductivity of the paste aggregate interface was measured by considering a twin geometrical model and assuming a 20 μm thickness of the ITZ (Ping et al. 1991). They concluded the conductivity of the ITZ is l0 times greater than that of the bulk cement paste. Brenton and his colleagues estimated the chloride diffusion coefficient of the ITZ. Their results show that the diffusion coefficient of the ITZ is approximately 12 times greater than that in the bulk cement paste (Breton et al. 1992).

Theoretical and experimental analysis has proven that higher porosity of the ITZ facilitates the diffusion (Delagrave et al. 1997). Furthermore, if the individual ITZs interconnect to percolate across a specimen, the transport properties of the specimen would be expected to change, since pathways or larger pores will then be available for faster fluid or ion transport (Bentz et al. 1995; Buenfeld et al. 1998). As can be seen, ITZ has significant impact on the properties of concrete and it is imperative to consider it in all modeling approaches (Garboczi et al. 1995; Garboczi et

al. 1996; Bentz et al. 1998; Buenfeld et al. 1998). The thickness of the ITZ varies due to different factors such as water-to-cement-ratio (Elsharief et al. 2003), addition of supplementary cementitious materials (Rangaraju et al. 2010), and aggregate size (Basheer et al. 2005). Most researchers considered the thickness of ITZ in the range of 20-50 μm (Hadley 1972; Bentz et al. 1994). In this study in all models, the thickness of the ITZ is assumed to be 40μm.

2.6. Corrosion of steel in concrete

Concrete gives corrosion resistance to steel reinforcement because it provides both a physical barrier and chemical protection. Steel is thermodynamically unstable in atmosphere and tends to revert to a lower energy state such as an oxide or hydroxide by reaction with oxygen and water. Concrete that is not exposed to any external influences usually has a pH between 12.5 and 13.5 (Hansson 1984). As shown in the Pourbaix diagram (Figure 2.6.1), which defines the range of electrochemical potential and pH, for H_2O-Fe system in the alkaline environment and at the potentials normally existing in the concrete, a protective passive layer forms on the surface of steel. This layer is an ultra-thin (<10nm), protective oxide or hydroxide film that decreases the anodic dissolution rate to negligible levels (Zakroczymski et al. 1985; Zakroczymski et al. 1985; Montemor et al. 1998; Carnot et al. 2002). Formation of passive film on iron begins with dissolution of the metal which produces electrons and the reduction of oxygen that uses those electrons. The ferrous ions from the anodic dissolution of iron are attracted to the cathodic part of the steel and combined with hydroxide ions from the cathodic reaction of oxygen and form the ferrous hydroxide. If this film exposed to the oxygen, other passive oxide layers such as Fe_3O_4 or Fe_2O_3 may form on the outer surface of the film. Therefore, the passive film can be consisted

of layers of ion hydroxide or oxides based on different oxygen content (Hoar 1967; Uhlig 1967; Marcotte 2001).

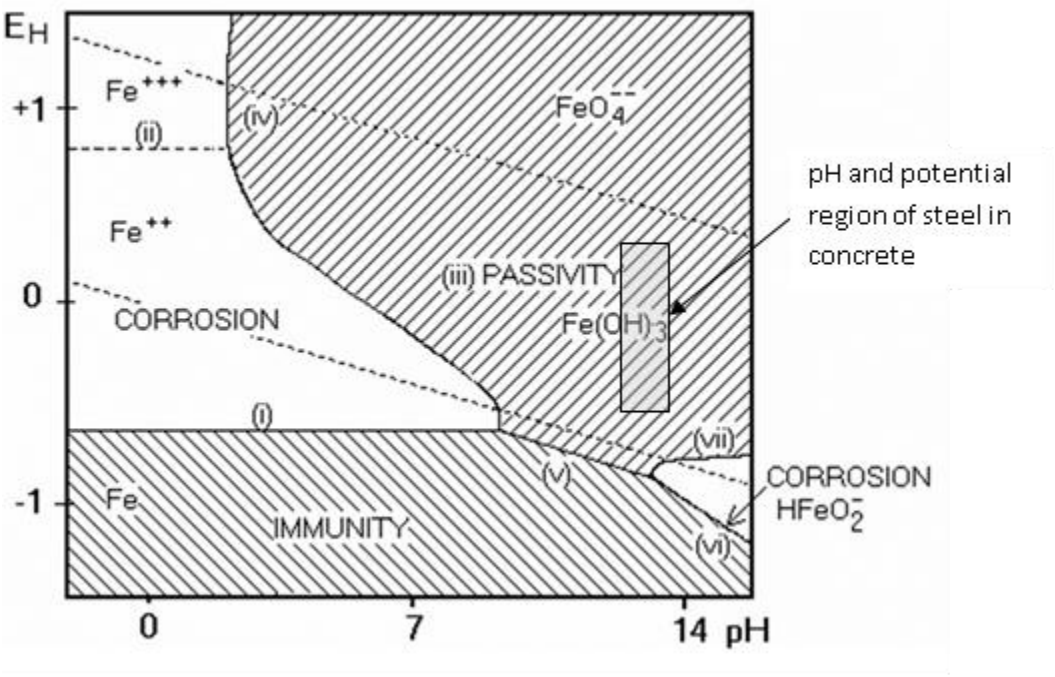

Figure 2.6.1. Pourbaix diagram for Fe-H_2O at 25^oC (Pourbaix 1974)

The protective nature of this layer can be reduced and the result would be active corrosion of steel in concrete. Chloride ions, mostly from de-icing salts or seawater, and carbon dioxide, from atmosphere, are two major factors that can break the passive film on the surface of steel and initiate corrosion.

Corrosion is an electrochemical reaction which consists of anodic and cathodic half-cell reactions. Micro-cell corrosion is the term given to the situation where active dissolution and the corresponding cathodic half-cell reaction take place at adjacent parts of the same metal part. For a steel reinforcing bar (rebar) in concrete, this process always occurs in practice. The surface of

the corroding steel can act as a mixed electrode containing both anode and cathode regions which are connected by the bulk steel. Macro-cells corrosion can also form on a single bar exposed to different environments within the concrete or where part of the bar extends outside the concrete. In both cases, concrete pore solution functions as an electrolyte. Figure 2.6.2 shows a schematic illustration of corrosion in reinforcing concrete.

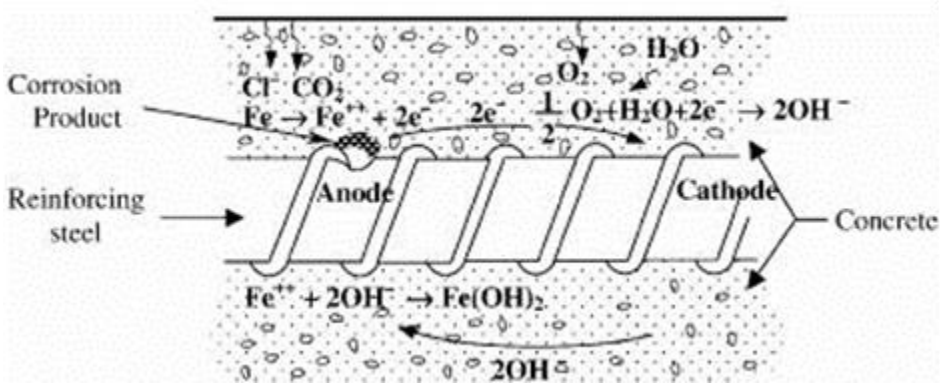

Figure 2.6.2. Schematic illustration of the corrosion of reinforcement steel in concrete (Ahmed 2003)

For steel embedded in concrete, based on the pH of the concrete (electrolyte) and presence of aggressive ions, the following would be the possible anodic reactions (Hansson 1984; Ahmed 2003):

$3Fe + 4H_2O \rightarrow Fe_3O_4 + 8H^+ + 8e^-$ (eq. 2.6.1)

$2Fe + 3H_2O \rightarrow Fe_2O_3 + 6H^+ + 6e^-$ (eq. 2.6.2)

$Fe + 2H_2O \rightarrow HFeO_2^- + 3H^+ + 2e^-$ (eq. 2.6.3)

$Fe \rightarrow Fe^{2+} + 2e^-$ (eq. 2.6.4)

The possible cathodic reactions depend on the availability of O_2 and on the pH near the steel surface. The most likely reactions are as follows (Hansson 1984; Ahmed 2003):

$$2H_2O + O_2 + 4e^- \rightarrow 4OH^- \quad \text{(eq. 2.6.5)}$$

$$2H_2O + 2e^- \rightarrow H_2 + 2OH^- \quad \text{(eq. 2.6.6)}$$

The corrosion products occupy a greater volume than the steel itself, and this causes an internal expansion and stress. The stress can destroy the concrete and expose the steel to more aggressive factors. Figure 2.6.3 shows a schematic illustration of a damaged concrete by corrosion of reinforcement steel.

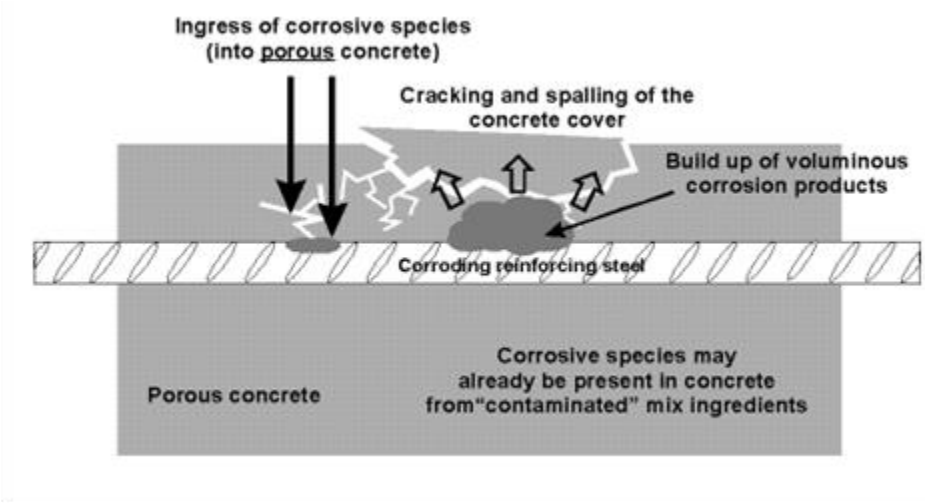

Figure 2.6.3. Schematic diagram showing spalling of concrete due to corrosion damage (Corrosion-club 2004)

Since corrosion due to chloride ions is the main mechanism of corrosion of steel in concrete in North America, this mechanism will be explained further in next section.

2.7. Chloride induced corrosion

Chloride ions can be present in the concrete due to the use of chloride contaminated components or the use of $CaCl_2$ as an accelerator when mixing the concrete, or by diffusion into the concrete from the outside environment (Thuresson 1996). A localized breakdown of the passive layer occurs when sufficient amount of chlorides reach reinforcing bars, and the corrosion process is then initiated. Chlorides in concrete can be either dissolved in the pore solution (free chlorides) or chemically and physically bound to the cement hydrates and their surfaces (bound chlorides). Only the free chlorides dissolved in the pore solution are responsible for initiating the process of corrosion (Pérez et al. 2000).

There are three theories about the chloride attack (ACI Committee 222 1996):

1. Penetration of chloride ions to the oxide film on steel through pores or defects in the film is easier than the penetration of other ions.
2. Chloride ions are adsorbed on the metal surface in competition with dissolved O_2 or hydroxyl ions.
3. Chloride ions compete with hydroxyl ions for the ferrous ions produced by corrosion and a soluble complex of iron chloride forms which can diffuse away from the anode, destroying the protective layer of $Fe(OH)_2$ permitting corrosion to continue.

2.8. Chloride diffusion in concrete

Many experimental works has been carried out to establish mathematical modeling for chloride diffusion in cementitious material. Collepardi and his colleagues studied the chloride diffusion

coefficient for different cement mixtures (Collepardi et al. 1967). Diffusion of chloride ions into concrete from seawater was also studied by Gjorv and Vennesland (Gjorv et al. 1979). Page and his colleagues found that increasing the water to cement ratio increases the diffusion rate of the chloride ions (Page et al. 1981). Midgley and his colleague showed that penetration of chloride ions at a given time increases with increasing the concentration of chloride ions (Midgley et al. 1984).The relative importance of the two major mechanisms of chloride transport, namely diffusion and absorption, depend on the moisture content of concrete. Absorption may be dominant if a dry concrete with significant loss of pore water is wetted with chloride-bearing water, whereas for a sufficient level of pore water diffusion process will prevail. However, researchers tend to agree that in most cases diffusion can be assumed to be the basic transport mechanism of chloride ions for reasonably moist structures (Wonga et al. 2010; Apostolopoulosa et al. 2013).

Diffusion occurs under a concentration gradient and it will take place if the concentration on the boundary is higher than inside of concrete. The chloride penetration can be modeled by Fick's diffusion law (Xi et al. 1999). Literature review shows that, several techniques have been used to find a solution to the partial differential equation for Fick's second law in the presence of appropriate boundary conditions. The commonly applicable form involves concentration of chloride ions at the exposed surface and at a distance from the surface, as it is conveniently measured as percentage (Weyers et al. 1989). Funahashi adopted a nonlinear regression analysis and a finite difference method was used by (Funahashi 1990). Midgley and his colleague pursued numerical integration and Liam used an iterative program to determine the value of diffusion coefficient which best fits the data of chloride concentration (Midgley et al. 1984; Liam et al.

1992). Nagano and Naito provided a solution to Fick's law with using periodic functions at the boundary (Nagano et al. 1985). Nagano and Naito modeled concrete as three-phase composite materials consisting of matrix phase, aggregate phase, ITZ and their homogenization phase (Nagano et al. 1985). Their model predicts that the chloride diffusivity of concrete composite materials depends on the chloride diffusion coefficient of the matrix, volume fraction of the ITZ and volume fraction and size distribution of the aggregate. In the study of diffusion in concrete performed by Zheng and Ahou, they considered concrete as three-phase composite model including; coarse aggregates, ITZ and cement paste. Range of ITZ thickness was considered between 0.02 and 0.05 mm. They found that ITZ thickness has the most important effect on chloride diffusivity while aggregate size and gradation are the least important factor on chloride diffusion (Zheng et al. 2008).

The diffusivity of chloride in several paste and exposure parameters has been examined using electron probe microanalysis (EPMA) by Jensen and his colleagues. They found that increasing water to cement ration increase chloride diffusivity (Jensen et al. 1999).

Previous investigations have used the finite element to model 2D chloride diffusion into saturated concrete (Pérez et al. 2001; Shin et al. 2002; Suwito et al. 2006; Zeng 2007; Zheng et al. 2008). Concrete has been considered as a homogeneous material in these studies, however; the influences of the ITZ and aggregates size and shape were disregarded.

Xiao and his colleagues modeled a two-phased concrete with coarse aggregate and cement paste (Xiao et al. 2012).The main focus of their work was on the effect of particles shape on chloride diffusivity. As can be seen in Figure 2.8.1., the chloride diffusion process is influenced by the

shape of aggregates and increasing the number of the members of the polygon decrease the diffusivity of chloride.

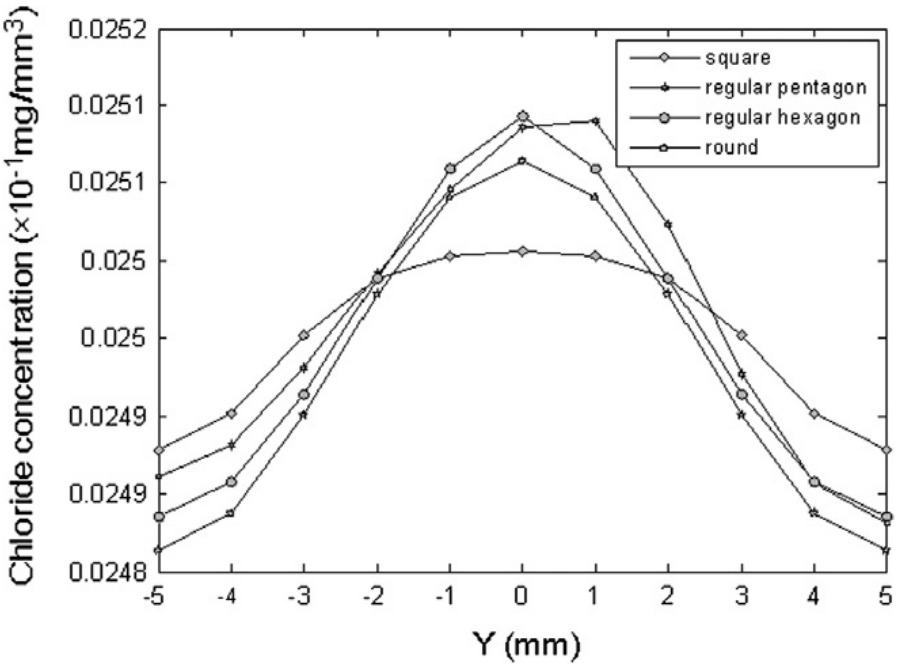

Figure 2.8.1. Comparison of chloride concentration using different shaped aggregate (Xiao et al. 2012)

Nevertheless, the effect of real shape and geometry of coarse aggregates, fine aggregates and air voids was not considered in their study.

2.9. Rate of diffusion

Adolf Eugen Fick (1829-1901) was the first scientist to provide a quantitative description of the diffusion process (Askeland et al. 2003). The rate at which atoms, ions, particles or other species diffuse in a material can be measured by the flux J. The flux J is defined as the amount of

substance passing through a plane of unit area per unit time (Figure 2.9.1). Fick's first law explains the net flux of atoms:

$$J = -D \frac{dc}{dx} \qquad \text{(eq. 2.9.1)}$$

Where J is the diffusion flux, D is the diffusivity or diffusion coefficient ($m^2.s^{-1}$) and, dc/dx is the concentration gradient ($mol.m^{-3}.m^{-1}$). Depending upon the situation, concentration may be expressed as percent.

The negative sign in Equation 2.9.1 indicates that the flux of diffusing species is from higher to lower concentrations, making the dc/dx term negative and hence J will be positive. The concentration gradient shows how the composition of the material varies with distance: Δc is the difference in concentration over the distance Δx. The concentration gradient may be created when a gas or liquid is in contact with a solid material. The flux at a particular temperature is constant only if the concentration gradient is also constant, that is, the compositions on each side of the plane remain unchanged. Often, the flux is initially high and then gradually decreases as the concentration gradient is reduced by diffusion.

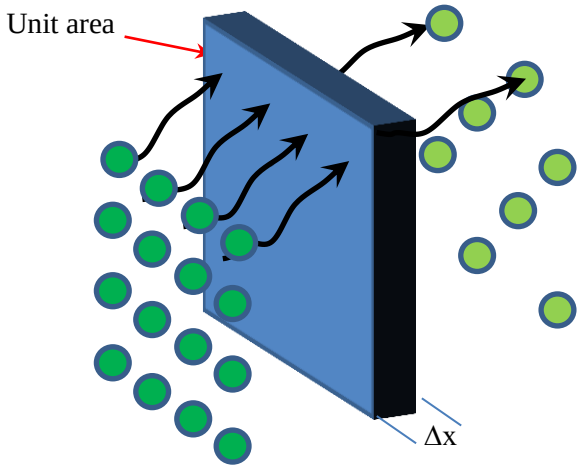

Figure 2.9.1. The diffusion flux is the number of atoms passed through the unit area of a plane per unit time

Fick's second law describes the dynamic or non-steady state diffusion; it derived from Fick's First law and the mass conservation in absence of any chemical reactions (Pérez et al. 2000; Yuan et al. 2009):

$$\frac{\delta c}{\delta t} = \frac{\delta}{\delta x}\left(D\frac{\delta c}{\delta x}\right) \qquad \text{(eq. 2.9.2)}$$

If it is assumed that the diffusion coefficient D is not a function of location x, and the concentration (c) of diffusion species, then a simplified version of Fick's second law can be obtained as following:

$$\frac{\delta c}{\delta t} = \left(D\frac{\partial^2 c}{\partial x^2}\right) \qquad \text{(eq. 2.9.3)}$$

For the case of diffusion in two or more dimensions Fick's second law becomes:

$$\frac{\delta c}{\delta t} = D\left(\nabla^2 c\right) \qquad \text{(eq. 2.9.4)}$$

The solution of equation 1.5.3.3 in simple case of diffusion in one dimension from a boundary located at position x=0, where the concentration is maintained at value C_s is (Crank 1979):

$$\frac{C(x,t)}{C_S} = 1 - erf\left(\frac{x}{2\sqrt{Dt}}\right) \qquad \text{(eq. 2.9.5)}$$

Where C_S is a constant concentration of the diffusing material at the surface, C(x,t) is the chloride content at the depth x at a given time. *erf* represents the error function, C_S is the chloride concentration at the top surface of the concrete.

2.10. Corrosion measurement techniques

As mentioned, corrosion consists of electrochemical reactions at the interface between the metal and an electrolyte solution. During the anodic reaction, a metal is oxidized and releases electrons. These electrons are consumed by the cathodic reaction in which the reduction occurs. By equating these two reactions, a corrosion current, I_{corr}, which is the absolute value of corrosion rate, and half-cell potential (also called corrosion potential or open circuit potential), E_{corr}, which is the probability of corrosion, can be found.

E_{corr} is the potential of the corroding object versus a reference electrode under no-load conditions (no potential or current is applied) and can be measured with a high impedance voltmeter or potentiometer (Elsener et al. 2003; Corrosion-doctors 2005). However, I_{corr} cannot be measured directly but it can be estimated by using electrochemical techniques while E_{corr} must be determined as the potential difference between that of the metal surface and a reference electrode. As mentioned, corrosion occurs via electrochemical reactions. Therefore, electrochemical techniques are ideal for the study of the corrosion processes.

Usually, in electrochemical measurements, a cell consists of a working electrode (the corroding metal), a counter electrode, a reference electrode and electrolyte. All of the electrodes are connected to a potentiostat which allows the potential of the metal to be changed in a controlled manner and the resultant current flow to be measured as a function of potential. This changing of the potential is called "polarization".

2.10.1. Half-cell potential technique

The half-cell potential technique is the most widely used technique of corrosion measurement of the steel rebars in concrete. It was introduced in the 1970s by Richard F. Stratfull in North America and by the Danish Corrosion Centre in Europe (Stratfull 1968; Stratfull 1972; FORCE Technology 2004) . In 1980, the test was approved as a standard by ASTM: C 876 "Standard Test Method for Half-cell Potentials of Uncoated Reinforcing Steel in Concrete". This technique is based on measuring the electrochemical potential of the steel rebar with respect to a standard reference electrode placed on the surface of the concrete and can provide an indication of the corrosion risk of the steel. The suggested reference electrode by ASTM is a copper/copper

sulphate electrode (CSE). A wet sponge should be placed between the electrode and the concrete to provide a low electrical resistance i.e. good contact between the electrode and the concrete. Figure 2.10.1, shows the basics of half-cell potential measurement.

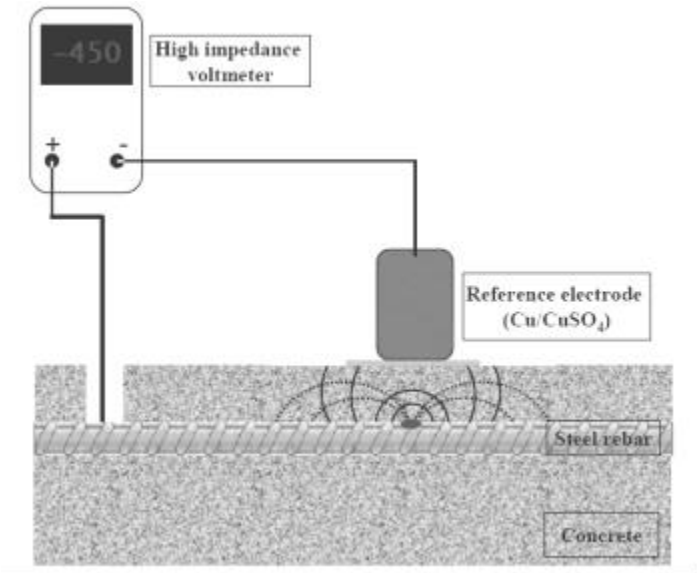

Figure 2.10.1. Apparatus for half-cell potential method described in ASTM C 876 to measure surface potential associated with corrosion current

According to the ASTM Standard, the recommended guidelines for interpretation are as follows:

Table 2.10.1. Probability of corrosion according to half-cell potential reading (ASTM 1999)

Half-cell potential reading vs. Cu/CuSO4	**Corrosion activity**
More positive than -200 mV	90% probability of no corrosion
Between -200 and -350 mV	An increase probability of corrosion
More negative than -350 mV	90% probability of corrosion

2.10.2. Linear Polarization Resistance (LPR)

Figure 2.10.2 shows a schematic plot of the relationship between potential and current in the region of the open circuit potential. The curve plots the applied potential versus measured current or vice versa. As shown in Figure 2.10.2, there is an approximately linear region in the region of the open circuit potential. LPR measurements are performed by applying a potential in the range of ±20mV about the E_{corr}, either as a constant pulse (potentiostatic) or a potential sweep (potentiodynamic) and measuring the current response. Alternatively, a current pulse (galvanostatic) or a current sweep (galvanodynamic) can be applied, and potential response is measured. Polarisation resistance (R_p) is the resistance of the specimen to oxidation while an external potential is applied and the corrosion rate which is inversely related to the R_p can be calculated from it (Princeton Application Research 2005).

R_p is determined by calculating the slope of this linear region:

$$R_p = \frac{\Delta E}{\Delta I} \qquad \text{(eq. 2.10.2.1)}$$

Where, ΔE = change in potential and ΔI = change in current.

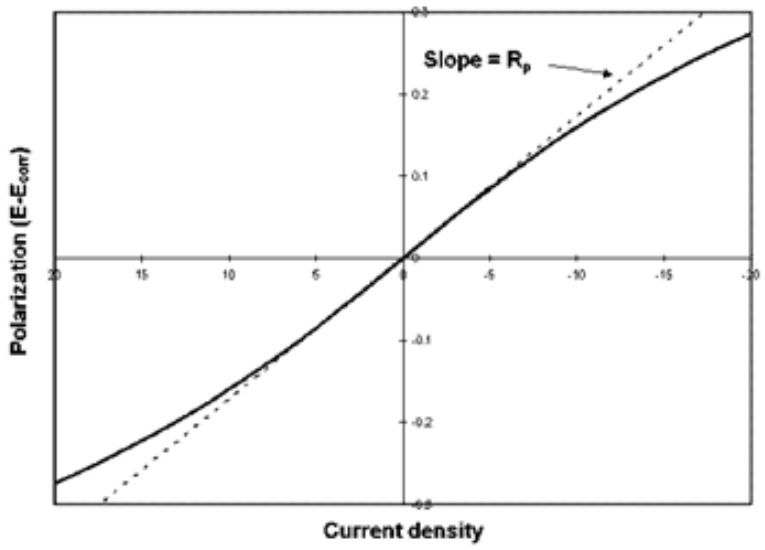

Figure 2.10.2. Linear polarisation curve (Corrosion-doctors 2005).

The Stern-Geary equation relates corrosion current to R_p (Stern et al. 1957):

$$I_{corr} = \frac{B}{R_p} \qquad \text{(eq. 2.10.2)}$$

$$B = \frac{\beta_a \beta_c}{2.3(\beta_a + \beta_c)} \qquad \text{(eq. 2.10.3)}$$

B is Stern-Geary constant and β_a and β_c are anodic and cathodic Tafel constants, respectively. The value of B is empirically determined and has been measured as 0.026V for active and 0.052V for passive corrosion of steel in concrete (Andrade et al. 1978; Andrade et al. 1990).

The resistance measured by LPR is actually is the sum of the polarization resistance, R_p, and the electrolyte resistance, R_Ω. Normally, $R_p >> R_\Omega$ and the resistance which is measured by LPR is

close enough to the polarization resistance that can be used as the actual value. However, in some environments with low conductivity, and/or high corrosion rates, the R_Ω is significant and should be considered (Jones 1992).

The corrosion current density, i_{corr}, can be calculated by dividing the corrosion current (I_{corr}) by the surface area of the polarised area (A):

$$i_{corr} = \frac{B}{R_p A} \qquad \text{(eq. 2.10.4)}$$

2.10.3. Potentiostatic LPR

In potentiostatic LPR technique, a constant potential signal (usually ±20mV) is applied for a certain period of time, which is determined by time for current to reach steady state, in the form of square wave between the working electrode (steel bar in concrete) and reference electrode and the response current (Δt in Figure 2.10.3) is measured. By using eq. 2.10.2.4, the R_P and consequently, corrosion current density and corrosion rate can be calculated.

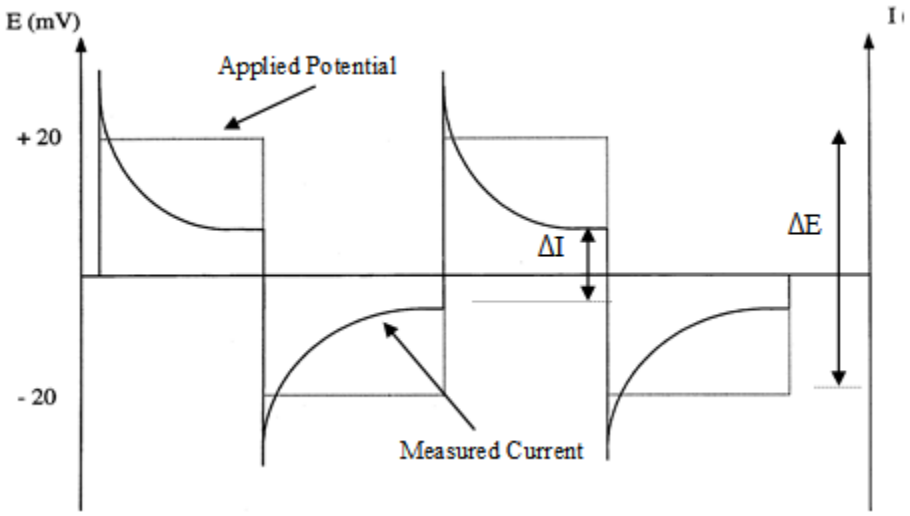

Figure 2.10.3. Applied potential and current response during LPR measurement

2.10.4. Cyclic polarization

Cyclic potentiodynamic polarization technique is a relatively non-destructive measurement that can provide information about the corrosion rate, corrosion potential, susceptibility to pitting corrosion of the metal and concentration limitation of the electrolyte in the system. The original test standard, ASTM G5 (ASTM 1999), was expanded from a stepped potentiostatic test to a potentiodynamic test as electronics developed, and consequently to a cyclic experiment (ASTM G 61 (ASTM 1998)) (Corbett). The technique is built on the idea that predictions of the behavior of a metal in an environment can be made by forcing the material from its steady state condition and monitoring how it responds to the force as the force is removed at a constant rate and the system is reversed to its steady state condition. Applied potential is the force and is raised at a continuous, often slow, rate by using potentiostat (Silverman). This rate is called polarization scan rate and is an experimental parameter.

The shape of the curve indicates if the sample is in the passive or active state, and can also show the pitting potential and the re-passivation or protection potential. In a passive system, the potential at which the current sharply increases is defined as the pitting potential (E_{pit}) and where the loop closes on the reverse scan is the protection or re-passivation potential (E_{pro}). If these two potentials are the same, there is a little tendency to pitting. If E_{pro} is more positive than E_{pit}, there is no tendency to pitting. On the other hand if E_{pro} is more negative than E_{pit}, the pitting could happen. Furthermore, the size of the pitting loop can be used as an indication of pitting tendency. The larger loop shows more tendency to pit (Princeton Applied Research). Figure 2.10.4 shows how the pitting or nucleation potential and re-passivation of protection potential can be deduced from the potentiodynamic cyclic polarisation curves.

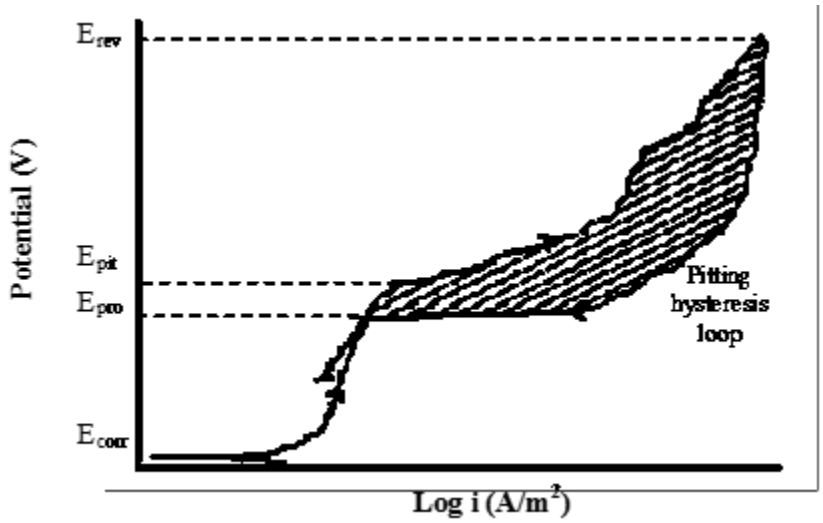

Figure 2.10.4. Schematic of pitting and passivation potentials on cyclic polarization curve (Princeton Applied Research))

CHAPTER 3: EXPERIMENTAL PROCEDURES

3.1. Sample preparation

For the experimental part of this project (both 2D and 3D), 100 × 200 mm concrete cylinders prepared according to ASTM C192, using the mixture proportions given in Table 3.1.2 and a w/c of 0.42. Type I ordinary portland cement with the composition summarized in (Table 3.1.1) was used to make all samples.

Table 3.1.1 Cement composition

Oxide	**%**	**Bogue Composition**	**%**
SiO_2	20.6	C_3S	58
Al_2O_3	5.1	C_2S	16
Fe_2O_3	3.4	C_3A	8
CaO	64.5	C_4AF	10
MgO	1.0	**Other Properties**	
SO_3	3.1	LOI, %	1.1
		Insoluble Residue, %	0.25
		Baline Fineness, m^2/Kg	391

After casting, cylinders were cured for 28 days and then CT scanning was performed on the samples.

In order to make chloride diffusion samples, the coarse aggregates were sieved and the half-inch portion was used as the maximum size of aggregate in the mix design.

Table 3.1.2. Mixture proportion

Materials	**Mass percentage (%)**
Cement	40
Fine aggregate	25
Coarse aggregate	35

3.2. 3D Image Processing

The Quantitative Computed Tomography (QCT) scans were carried out on cylinders using a clinical scanner (Philips MX 8000), at the Oconee Medical Center. The X-ray parameters were set at 120keV and 200mA. Each voxel has the size of 0.25 × 0.25 mm/pixel resolution, and 1mm slice thickness. This set up provides approximately 200 sliced pictures for each sample. Figure 3.2.1 shows one of the slices.

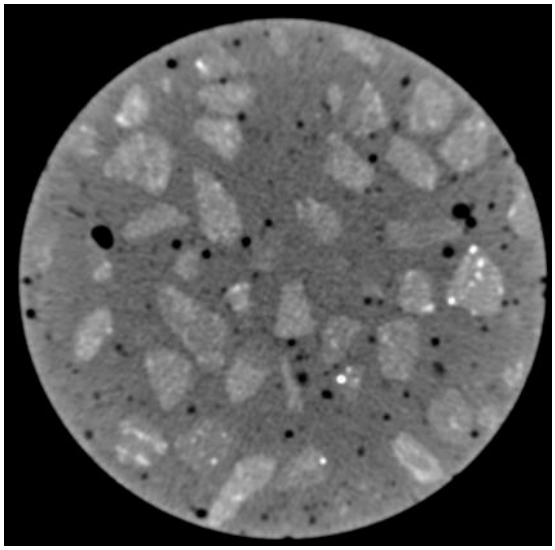

Figure. 3.2.1 One slice (image) taken by the QCT from the concrete cylinder

Images have some undesirable portion including some part of QCT sample holder. The first step was eliminating this portion. For this purpose a computer code was developed in MATLAB for the segmentation of concrete samples in every QCT slice. The unwanted portion of the image (shown in Figure 3.2.2.a) was removed by defining, a circular region of interest (ROI) in each QCT slice corresponding only to the concrete perimeter. (Figure 3.2.2. b)

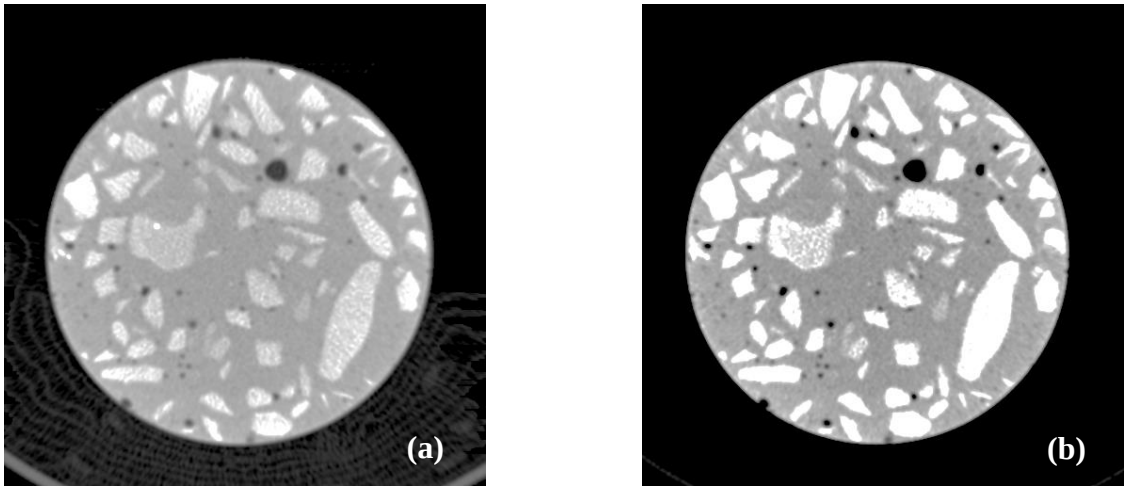

Figure. 3.2.2 QCT image of one of the slices (a) raw image showing the sample holder at the bottom, (b) processed image to eliminate unnecessary portions.

After that, fluctuation of pixels was reduced by applying a smoothing Wiener filter. Fluctuation always exists in X-ray images due to the diffractive nature of attenuation. The image in Figure 3.2.3 (a) shows the ideal model for detecting edge when intensity of images changes stepwise. In this situation, the edge will be a clear thin line. However, in reality, as Figure 3.2.3 (b) illustrates, images show a color gradation (fluctuation in intensity) which makes edge detection problematic.

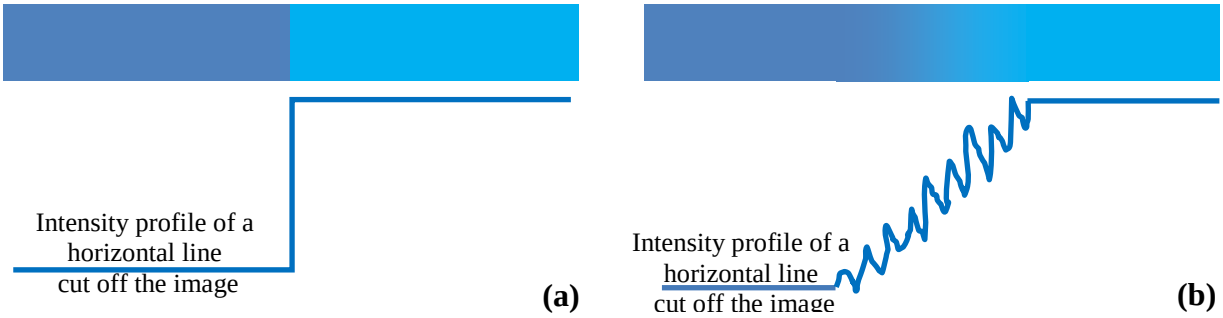

Figure. 3.2.3 (a) Model of an ideal digital edge, (b) Model of a noisy digital edge.

The Wiener method is the optimal restoration pixelwise adaptive technique based on statistics estimated from a local neighborhood of each pixel (Jahne 2004). This method uses a neighborhood of size m × n to estimate the local image mean and standard deviation to reduce the noise and fluctuation as well as minimize the error between the true image and the reconstructed result. Wiener estimates the local mean and variance around each pixel, using equations 3.2.1 and 3.2.2, respectively:

$$\mu = \frac{1}{NM} \sum_{n_1, n_2 \in \eta} a(n_1, n_2) \qquad \text{(eq. 3.2.1)}$$

$$\sigma^2 = \frac{1}{NM} \sum_{n_1, n_2 \in \eta} a^2(n_1, n_2) - \mu^2 \qquad \text{(eq. 3.2.2)}$$

where $a(n_1, n_2)$ is a two dimensional image, n_1 and n_2 are rows and columns and η is the n × m local neighborhood of each pixel in the image.

Wiener then creates a pixelwise filtered image, $b(n_1, n_2)$, using these estimates from equation 3.2.3:

$$b(n_1, n_2) = \mu + \frac{\sigma^2 - v^2}{\sigma^2}(a(n_1, n_2) - \mu) \qquad \text{(eq. 3.2.3)}$$

Where v^2 is the noise variance which could be the average of all the local estimated variances. The principle of Wiener filtering is schematically is shown in Figure. 3.2.4.

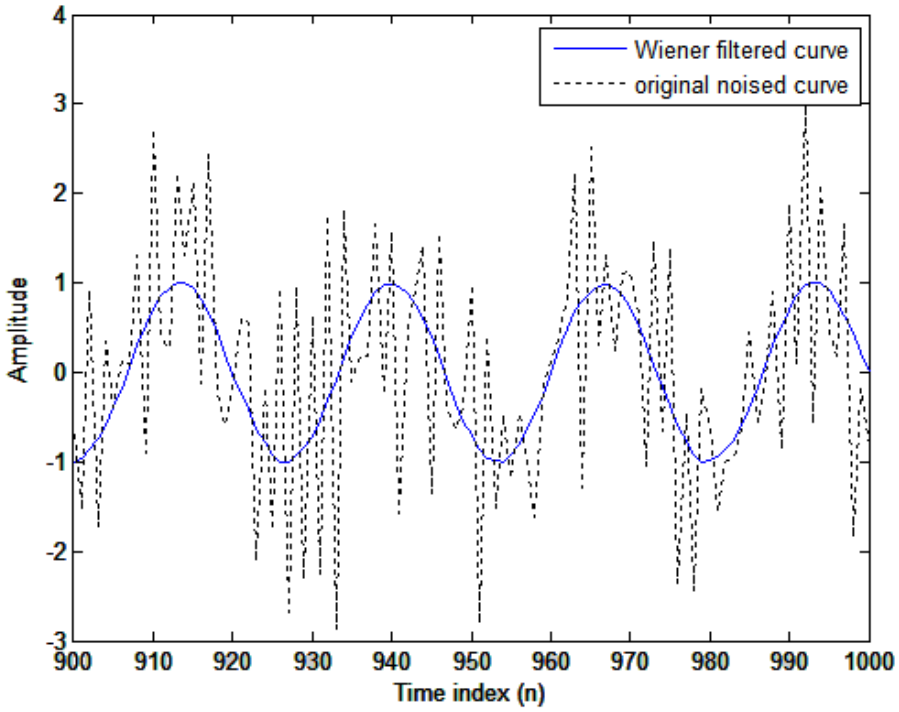

Figure. 3.2.4 Applying filter to noisy curve (MATLAB 2012).

The next step, after reducing and smoothing the fluctuation of pixels, is edge detection. Edge detectors provide a set of edge pixels which are combined into more elaborate primitives. An edge detector accepts digitized images as input and produces an edge map as output. The edge

map includes explicit information about the position and strength of edges, their orientation, and the scale. To detect an edge, a set of mathematical methods are required to identify points in a digital image at which there are changes in the image properties. By applying an edge detection algorithm to an image, the amount of data to be processed is significantly reduced and may, therefore, filter out less relevant information while preserving and restraining the important structural properties of an image to some regions. Canny is one of the best edge detection algorithms which was selected in this research. The Canny algorithm finds edges of the image by looking for gradient direction and local maxima of the gradient magnitude (Ziou et al. 1998). The gradient magnitude is nonlinear and invariant to rotation and can be calculated using the derivative of the image from equation 3.2.4 and will detect strong and weak edges.

$$|\nabla a| = \sqrt{(\frac{\delta a(n_1, n_2)}{\delta x})^2 + (\frac{\delta a(n_1, n_2)}{\delta y})^2} \qquad \text{(eq. 3.2.4)}$$

Weak edges are included in the output only if they are connected to strong edges. The gradient direction is perpendicular to the edge and is calculated from equation 3.2.5 to localize edges.

$$\varphi = arctg(\frac{\delta a(n_1, n_2) / \delta y}{\delta a(n_1, n_2) / \delta x}) \qquad \text{(eq. 3.2.5)}$$

The edge of the concrete sample in each image was detected automatically, using the abovementioned algorithm. Then, tangential filtering was used to enhance contrast between the image background and coarse aggregates. Figures 3.2.5a and 3.2.5.b show images before and

after applying the tangential filter, respectively. As shown in Figure 3.2.5a, before applying the filter some portion of aggregates have weak intensity that deteriorate its boundary line while applying filter(s) improved the image significantly (Figure 3.2.5b). As can be seen, weak portions of the image are improved and are ready for discrimination by detecting their edge. At the end of this step the segmented voxel based image was saved in the Digital Imaging and Communications in Medicine (DICOM) format.

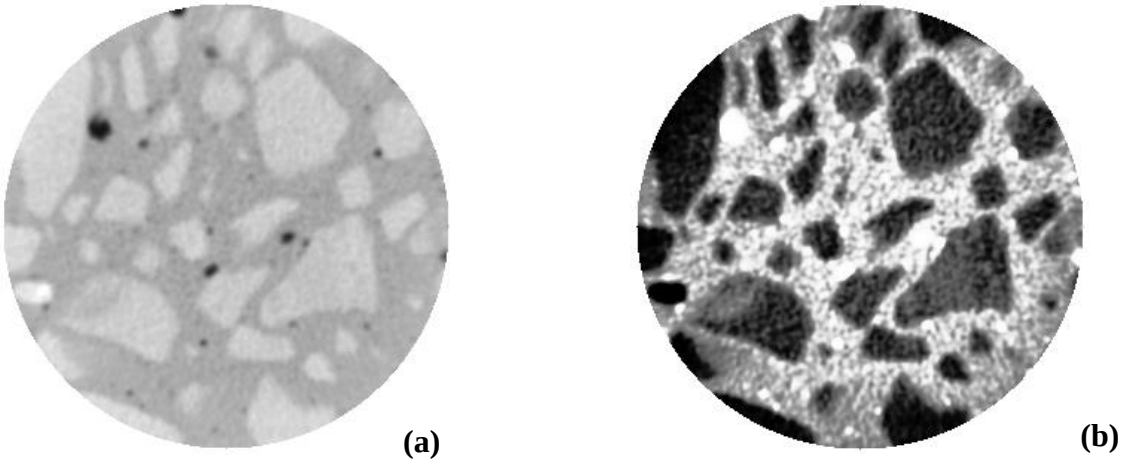

Figure. 3.2.5 QCT image of one of the slices (a) Original image after elimination surrounding, (b) processed image after applying sharpening filter

3.2.1. Aggregates discrimination

Coarse aggregates have a major role and influence in concrete properties. A significant volume of the concrete is occupied by coarse aggregates which bind together with cement paste. Changes in gradation, shape, and size, of the coarse aggregates can have substantial impact on the workability, strength, modulus and permanent deformation and ultimately the durability of the concrete. Therefore, computing volume and distribution of coarse aggregates in hardened concrete are important in this regard.

To recognize the coarse aggregates within the QCT images, identifying a line around them was necessary. This line compensates for the effect of discontinuity in the border of aggregates prepares the image for meshing in the finite element modeling. For this purpose, it was first necessary to define thresholds for each element which constrains the aggregates and ensures the independency of aggregates. Then, filtering techniques were used to adjust and enhance the image contrast. It should be mentioned that applying filters makes edges uniform due to a reduction of the fluctuation of image intensity, as illustrated in Figure 3.2.1.1. Uniformity and smoothness can be seen in Figure 3.2.1.1.b after applying suitable filters.

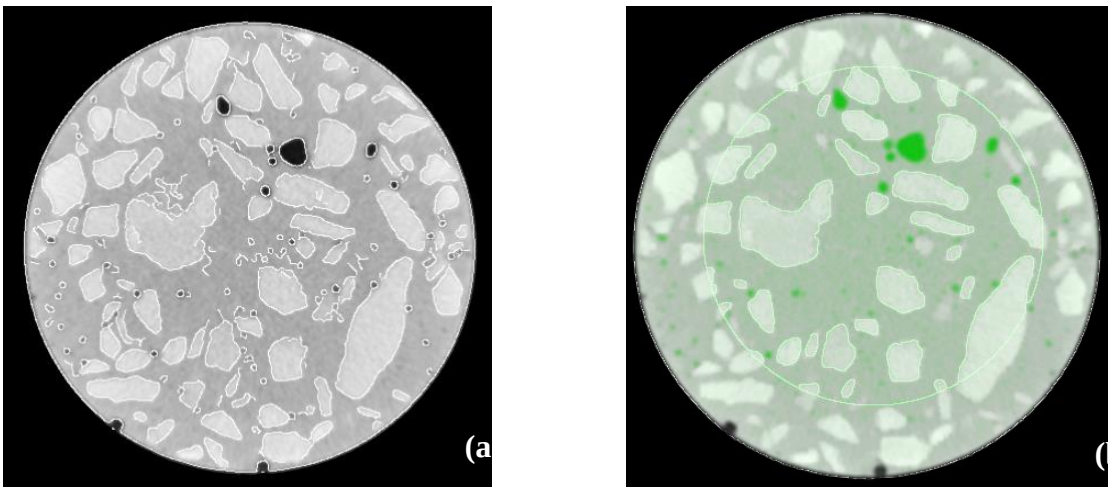

Figure. 3.2.1.1 A CT scan image (a) just with edge detection filter, and (b) after applying more filters to close all lines around the aggregates circumference

A difficulty often arises in dealing with objects within images because objects might touch and interact with each other and, therefore, cannot be separately identified, counted, or measured. The method that is usually preferred to separate touching features in an image is known as watershed segmentation which was used by Sun and his colleagues in 2009 to separate binary

particles in microscopic image processing (Sun et al. 2009). This method is schematically shown in Figures 3.2.1.2 to 3.2.1.6. First, the nearest distance between each pixel of the touched objects (Figure 3.2.1.2) and the background pixel is calculated. This distance is calculated by a straight line distance from each pixel of image to the nearest background pixel, as illustrated in Figure 3.2.1.3. Then, a distance map for two touched objects from the aforementioned calculations is constructed as shown in Figure 3.2.1.4. This distance is then converted to equivalent height, as shown in Figure 3.2.1.5. The ultimate points are the peaks of the mountains, and where features touch, the flanks of the mountains intersect. The saddles between these mountains are the lines selected as boundaries by the segmentation method. They are locations where water running down from the mountains arrives from two different peaks, and hence are called watershed lines. The placement of these lines according to the relative height of the mountains gives the best estimate of the separation lines between features, which are divided according to the regions that belong to each mountain top. Figure 3.2.1.6 shows two objects and the lines of separation by ridges between them.

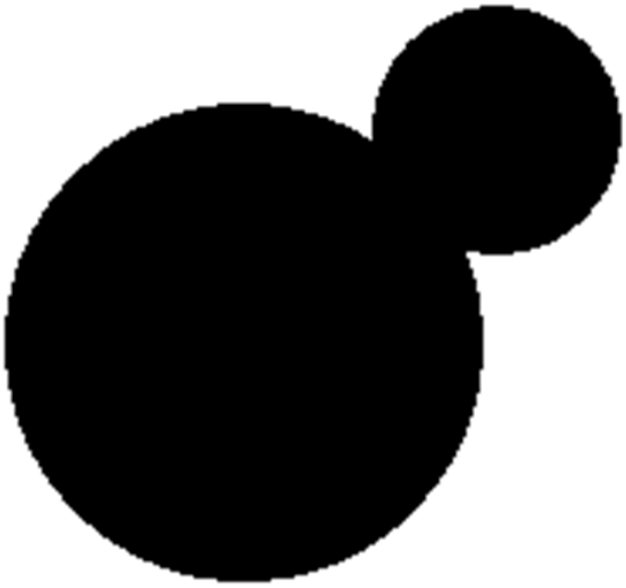

Figure 3.2.1.2. Binary image of two touching component

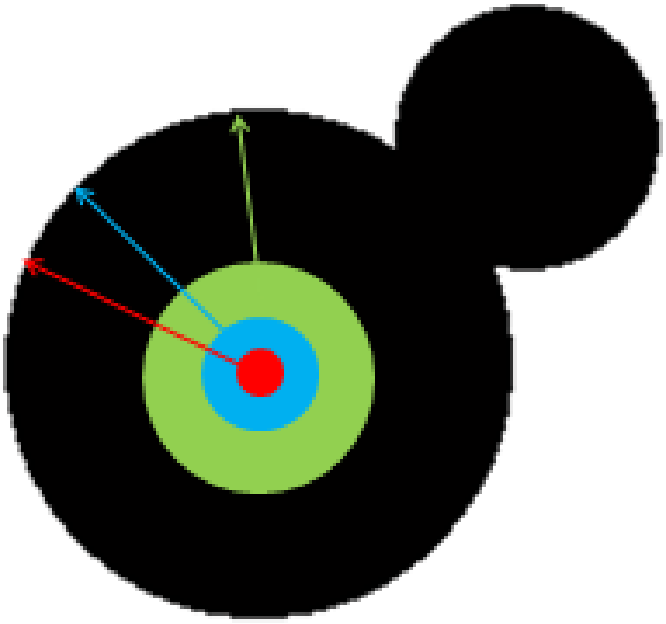

Figure 3.2.1.3. Euclidean distance map (EDM): straight line distance from the nearest background pixel

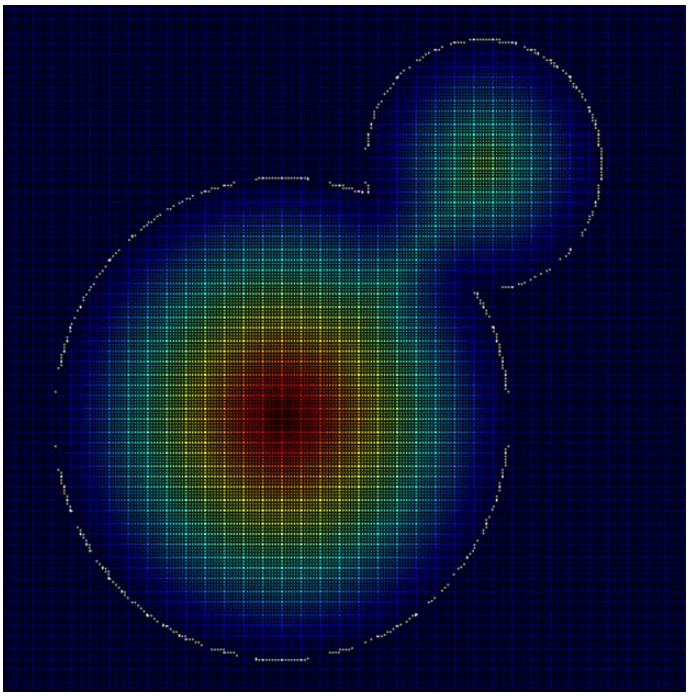

Figure 3.2.1.4. Euclidean distance map (EDM) applied on touched binary image

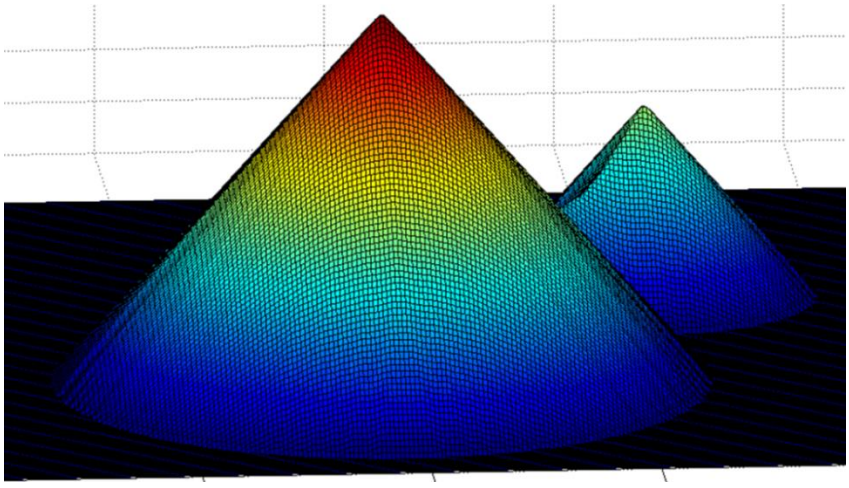

Figure 3.2.1.5. Applying heights to EDM of touched binary image

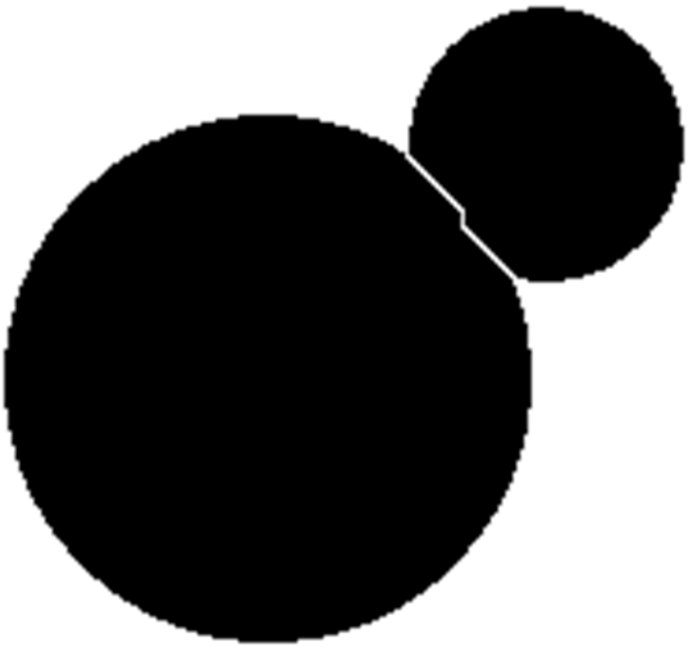

Figure 3.2.1.6. Applying watershed segmentation method to separate touched component

Applying this method separates the aggregates and provides different colors to aggregates indicating that they are recognized as separated different segments as shown in Figure 3.2.1.7 b. After the aggregate separation step, the percentage of volume fraction and distribution of aggregates in each slice section and in total volume of each sample can be calculated. Results from this approach were in very good agreement with the pre-determined amount in the mixture design.

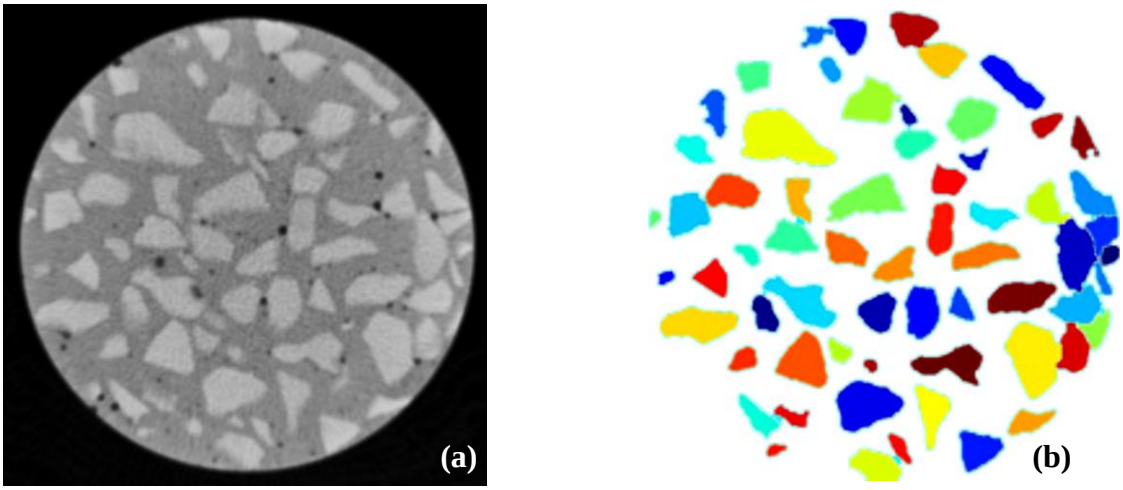

Figure. 3.2.1.7 Using watershed method for segmenting coarse aggregates. (a) Original QCT image and (b) watershed image. Different color indicates they are recognized as different segments

3.2.2. Air voids

It is well established that air voids play an important role in the durability of concrete. The higher air contents generally indicate larger bubble sizes and excessive amounts of air will drastically lower the strength of concrete (Mindess et al. 2003). By considering this matter, it is important to accurately calculate the size and distribution of air bubbles all over inside the sample instead of average amount of air content in some part of the sample. Most of the previous investigations were unable to distinguish between different sizes of air voids and they were focused on the total air content in concrete due to limitations in the laboratory techniques (Mindess et al. 2003), (Jakobsen et al. 2006) and (Kim et al. 2012). However, specimens with the same total volume of air voids may have different distributions of air voids, and consequently exhibit distinct mechanical properties. Thus, it would be of considerable interest to capture the air void distribution as well as its total volume. In the present study, QCT along with image analysis techniques was used to capture the air void distribution in concrete.

Air void content for each sample was determined by using the thresholding method. Most of the voids have irregular shapes. Therefore, a circle with equivalent surface area to each void was considered to identify the size of the void. Then the diameter of the circle was used as the size of the void (Ritter et al. 2009). It is imperative to emphasize that, after developing the required code and program, computing three dimensional volume, size and distribution of air voids in 100 × 200 mm cylindrical concrete sample takes approximately 5 minutes which compared to the conventional method, is considerably shorter. Additionally, more information, especially in 3D, can be obtained using this proposed method.

3.2.3. 3D Finite element modeling

Using QCT images to create an FEM model as close to the real concrete structure as possible, is proposed in this study. In this method, the geometry was obtained directly from the images without using any surface or solid body and the finite element mesh was developed by assigning hexahedral elements (0.25 × 0.25 × 1 mm) that each enclosed a predefined cubic volume of image voxels.. Figures 3.2.3.1 and 3.2.3.2 show one slice and the three-dimensional FEM of one of the cylinders, generated with a computer code developed in MATLAB, respectively.

During this study, it was realized that the conventional CT-scanner is not capable to identify the fine aggregates in the concrete and due to the resolution limitation of QCT, fine aggregate and cement paste were captured as a uniform matrix.

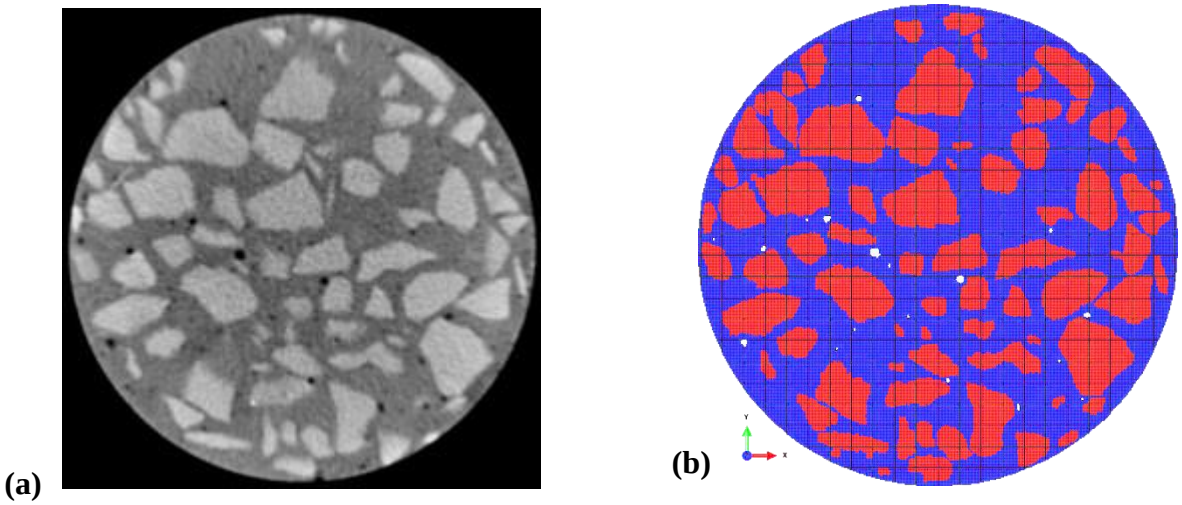

Figure. 3.2.3.1(a) A slice of concrete QCT image including coarse aggregates, voids and concrete matrix, (b) finite element model corresponding to the same slice

The other issue regards to creating a 3D FEM of the whole concrete cylinder (100 × 200 mm) is the number of elements and nodes which are 26 million and 27 million, respectively. Due to this high amount of elements using a personal computer for modeling and analysis is practically impossible. To overcome this problem, the Clemson high performance computing (HPC) resource was used for the calculations. However, regardless of the technical problems with the system, in the case that everything was going well, the modeling process of one cylinder was taking approximately one week to finish. Therefore, due to the difficulties that arose from image resolution and analysis of the model, this aspect of the modeling was not pursued during the rest of this study.

Figure. 3.2.3.2 Three-dimensional FEM of one of the cylinders

3.3. 2D imaging and modeling

Due to the problems from 3D FEM, explained previously, 2D FEM was used to study the chloride diffusion in concrete.

3.3.1. Sample preparation, surface preparation and flatbed scanning

A 50 x 100 mm sample was cut from the cylinder with a water-cooled diamond saw. The surface of the cut sample was in a plane perpendicular to the end surfaces of the cylinder. One surface of the sample was ground and polished by using a water-cooled lapping wheel with various size grit metal-bonded diamond platens. First, the sample was ground using a series of diamond abrasive particles. Then, it was gradually polished to 1200 grit with SiC paper. After each step, the sample

was rinsed with water and blown with compressed air to remove any residue from the previous grinding and polishing step.

An ordinary flatbed desktop scanner was used with a 2400 dpi optical resolution. The prepared sample was placed on the flatbed scanner and scanned in 24 bit RGB color at 2400 dpi. After that the coarse aggregates were painted by black marker to be detectable by the scanner and then scanned again. Next, the whole sample was painted black using a wide tipped black permanent marker. After the ink dried, a few tablespoons $Ca(OH)_2$ white powder was spread on the surface with the flat face of a glass slide. Then, the excess powder was scraped away with a razor blade. The remaining powder was wiped away with a lightly wet sponge, leaving only the powder pressed into the voids. The black and white surface was scanned. Then the sample was polished lightly to, remove color from the aggregates. Coarse aggregates were colored by black marker again while fine aggregates remained uncolored. This helped detecting fine aggregates precisely by scanner. The polished surface was scanned again in order to detect fine aggregates.

Since a sample was scanned several times, the images were not perfectly aligned. The coordinates of the corners in one image were correlated with the coordinates of the same points in another image, and used to align the images. The image processing toolbox in the Matlab software was used for the image alignment procedure and all subsequent image processing described later in the following section.

3.3.2. Image discrimination and classification

The image including coarse and fine aggregates and the image with voids were combined to make a binary image with high contrast between the air voids, cement paste, and aggregate. Figure 3.3.2.1 shows the original scanned image.

To detect the coarse aggregates, as abovementioned, first all of coarse aggregates in the sample painted with permanent black marker then scanned with flatbed scanner.

Then the scanned image was imported to Matlab and by adjusting threshold, black colored coarse aggregates were detected and separated from the original image.

Then the color intensity of the coarse aggregates was changed to one and saved in a separate file. Figure 3.3.2.2 (a) shows a sample with the coarse aggregates painted in black and Figure 3.3.2.2 (b) shows the binary image with detected coarse aggregates.

Figure 3.3.2.1. A 50 by 100 mm image (1250 x 2500 pixel) from the flat bed scan of the original surface

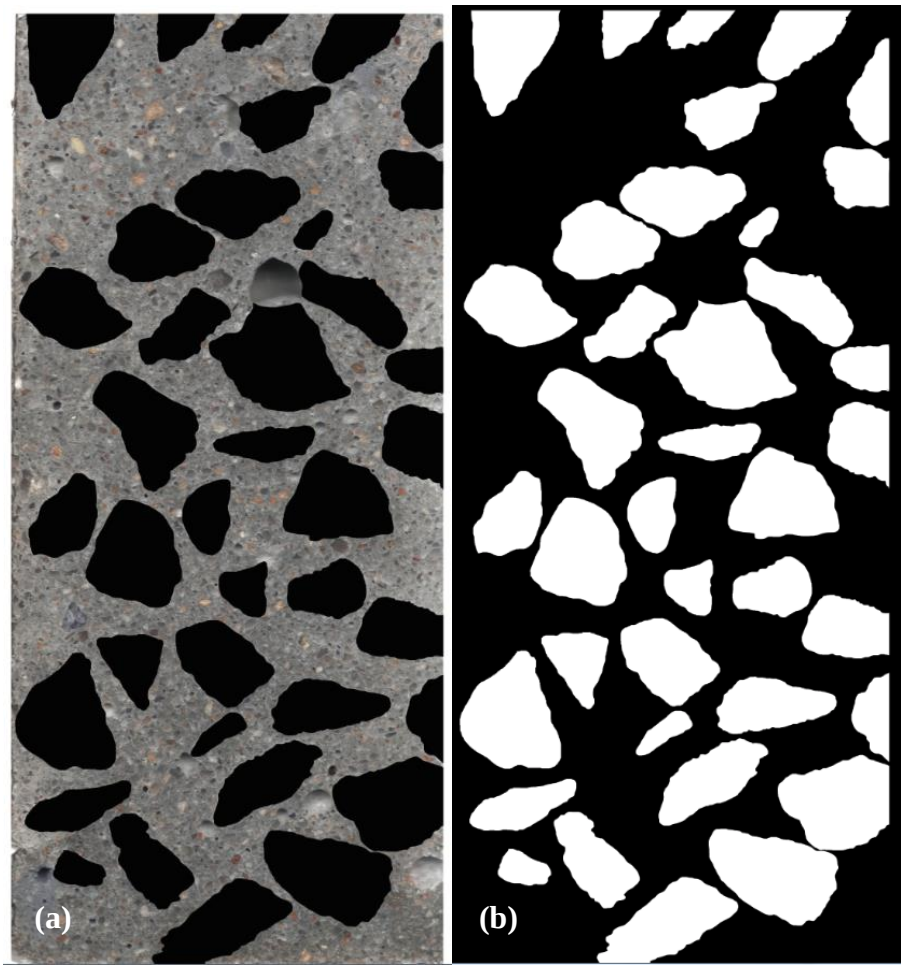

Figure 3.3.2.2. (a) Coarse aggregates painted in black and scanned, (b) Detected aggregates in white color

Figure 3.3.2.3 (a) shows the painted surface of the sample filled with white powder to detect air voids. The contrast between the black background and white powder helped to detect air voids from the image. This was done by removing pixels by applying the black threshold in Matlab. Figure 3.3.2.3 (b) shows the separated binary air voids. The pixel intensity number was changed to two and saved as a separate file.

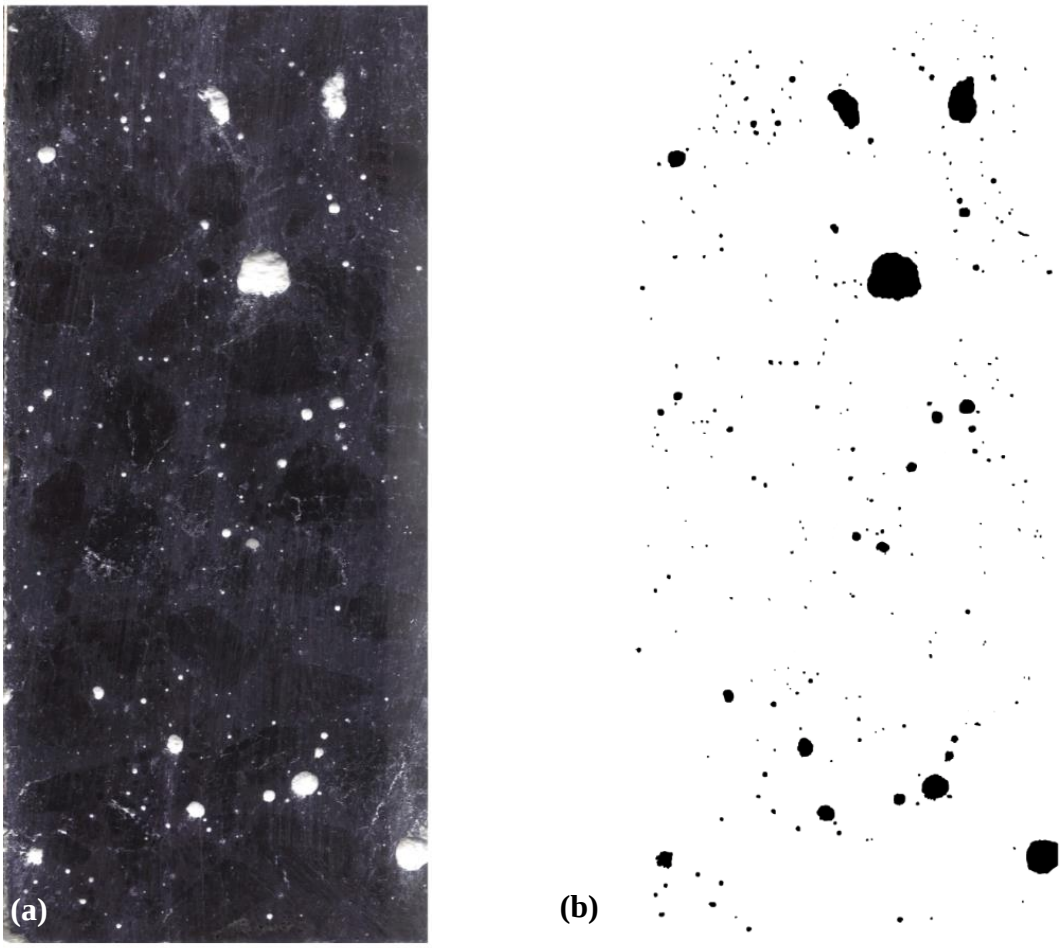

Figure 3.3.2.3. Images of; (a) Filled void with powder, (b) Detected voids in binary mode

After this step, as mentioned before, the surface of the sample was slightly polished and the fine aggregates were then revealed as shown in Figure 3.3.2.4 (a). The procedure explained before used in Matlab to remove the black background. The pixel intensity number was changed to three and saved as a separate file. Figure 3.3.2.4 (b) shows separated binary fine aggregates.

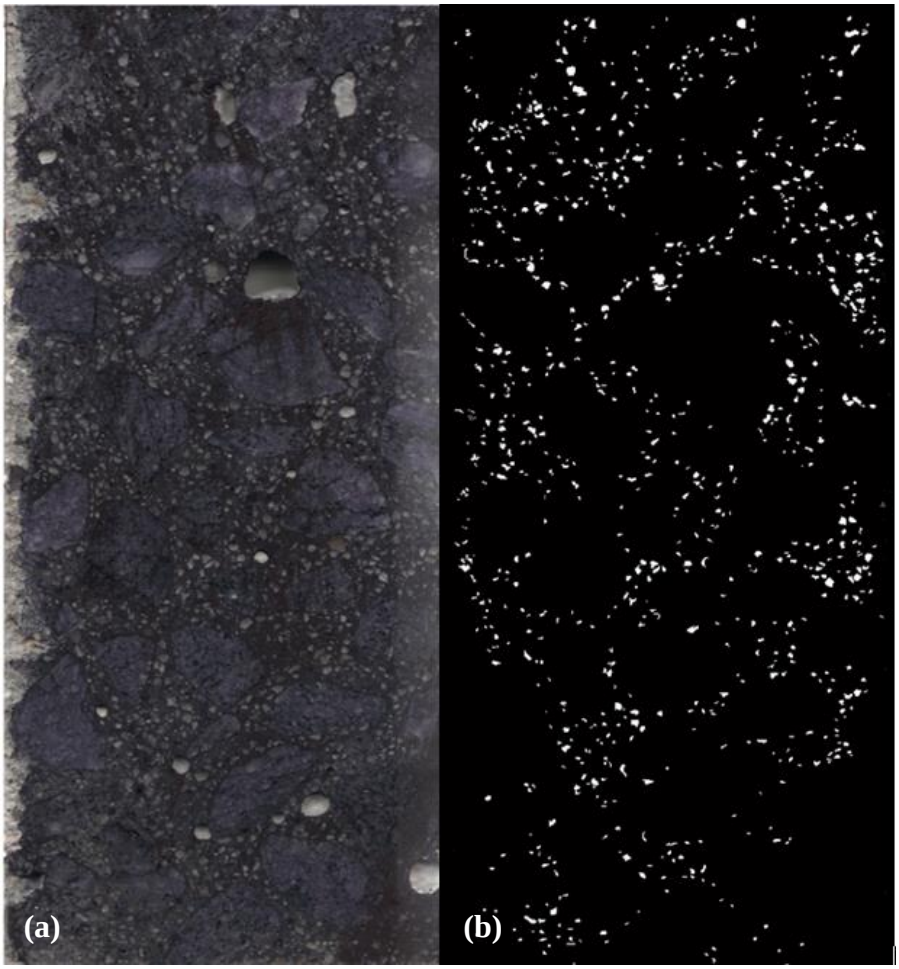

Figure 3.3.2.4. Images of; (a) Fine aggregates painted, polished and scanned, (b) Detected fine aggregates in black color background

The cement matrix was also separated in Matlab and a pixel intensity of 4 was assigned to it. All binary images were then combined into one image by applying a Boolean operation in Matlab. Figure 3.3.2.5 shows the merged image which contains; coarse aggregates (intensity one), air voids (intensity two), fine aggregates (intensity three), and cement paste (intensity four). Assigning different intensities to each phase facilitates specifying different materials to each phase later in the modeling process.

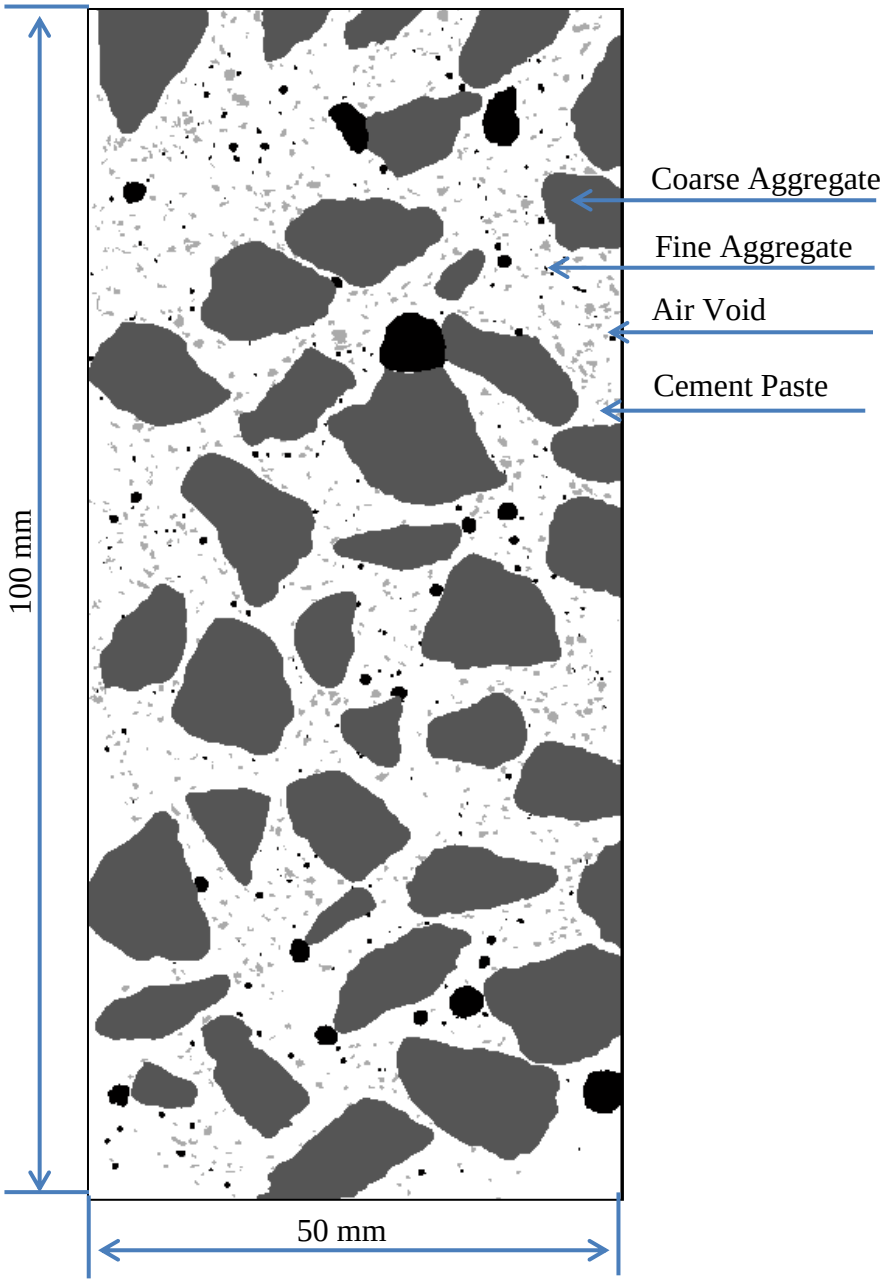

Figure 3.3.2.5. Final classified image including four phases; coarse aggregates, fine aggregates, voids and paste, each one has its own intensity number

3.3.3. Finite element modeling

The finite element model of the processed image was created in Abaqus software. The 2D DC2D4 quadrilateral diffusion element corresponding to diffusion analysis was selected and used in the model as shown in Figure 3.3.3.1.

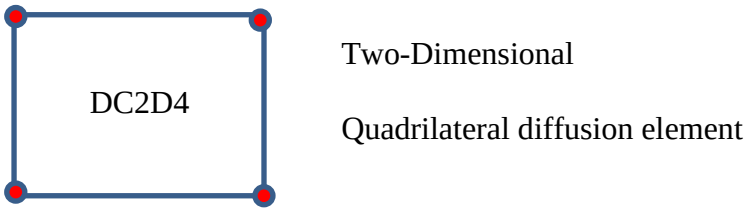

Figure. 3.3.3.1. ABAQUS two dimensional diffusivity elements used for analysis model

Each image was divided into approximately 3 million of these elements.. An element around each particle of coarse and fine aggregates has been considered as ITZ. The resolution of the image provides 0.04mm to each element which sufficiently represents the ITZ (Hadley 1972; Bentz et al. 1994).

Figure 3.3.3.2 and Figure 3.3.3.3 show the ITZ around coarse and fine aggregates, respectively.

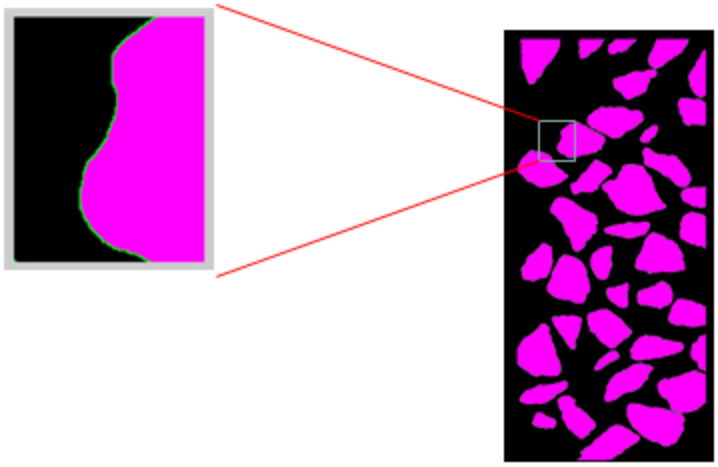

Figure. 3.3.3.2. ITZ around coarse aggregates

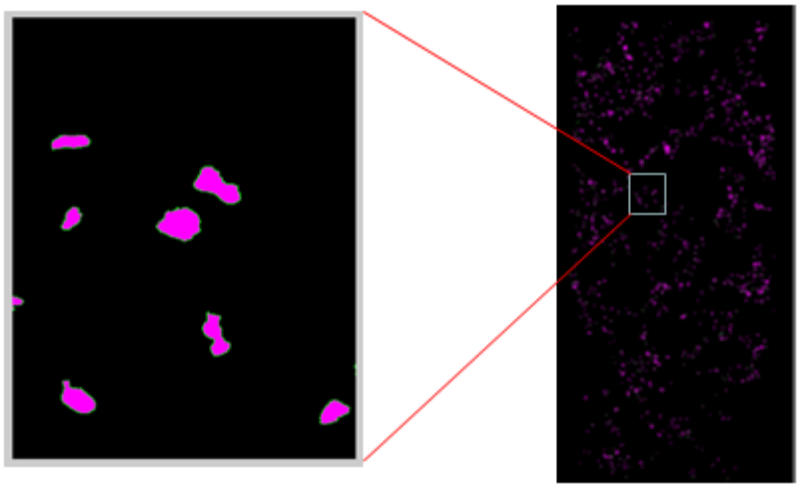

Figure. 3.3.3.3. ITZ around fine aggregates

To study the impact of the ITZ on chloride diffusion, three different models were prepared: (i) without ITZ, (ii) ITZ considered only around coarse aggregates and (iii) ITZ considered around both coarse and fine aggregates.

To each element of the meshed model, a material property corresponding to its intensity number was assigned. For example, to elements corresponding to intensity four, property of cement paste was specified.

Boundary conditions similar to the experimental setup were applied to the model: top surface is exposed to the chloride solution and the left, right and bottom sides are imposed with zero gradient of concentration as shown in Figure 3.3.3.4. Diffusivity through aggregates may be disregarded, as it is negligible compared to the transport in the matrix and through the ITZ (Ost et al. 1966).

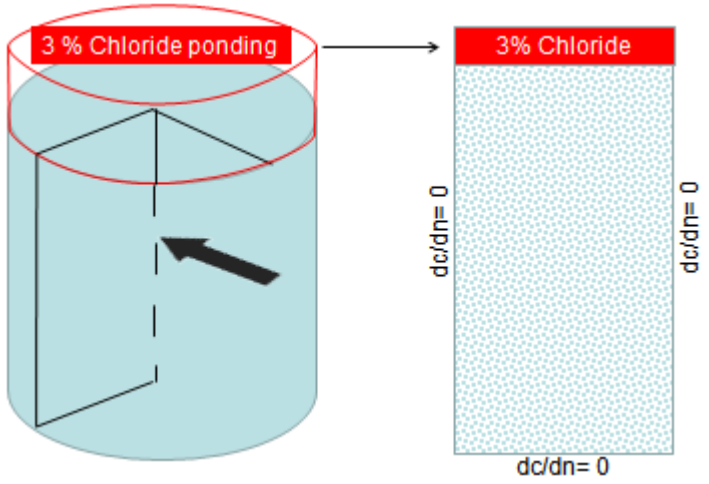

Figure 3.3.3.4. Boundary condition applied on the FEM

After applying boundary conditions, the chloride diffusion was molded and the results are shown in chapter 4.

CHAPTER 4: RESULTS AND DISCUSSION

4.1. Air void analysis

To validate the air void analysis performed by the CT scan image processing technique, the air voids of the samples were also measured according to ASTM C 457 Procedure B (ASTM 2011). This procedure was used to determine the air, paste, and aggregate contents, using eq. 4.1.

$$\text{Air content } \% = \frac{No.of\ AIR\,counts}{Total\ POINT\,count} \times 100 \qquad \text{(eq. 4.1)}$$

The method operates by determining whether a point should be classified as air, paste, or aggregate. Analysis occurs along a series of points in a grid system. The advantage of using a modified point count is determining the paste and aggregate content of concrete, in absence of a mixture design, which is required in most forensic petrographic examinations (ASTM C856, 2004).

In order to show the change in the air void content and distribution in different portions of the concrete cylinder, the sample was divided into two parts: upper and lower. From each part, sections were prepared and air void analysis was performed according to ASTM C457 (ASTM 2011). One of the disadvantages of this method is that the output gives the total air content in the surface (2-D) of the concrete slice. Furthermore, this method is very time consuming and its accuracy is based on the operator.

Void measurement on QCT images was also executed by the codes developed during this project. The distribution based on void size and frequency can be easily and rapidly calculated. Figure 4.1.1 shows the void distribution of one of the concrete cylinders. On this Figure, the horizontal axis shows void size groups and vertical axis shows void frequencies. Grouping numbers is shown in Table 4.1, as it indicated the void sizes range from less than 0.1 mm to greater than 1.0 mm.

Table 4.1. Air voids size grouping

Group Number	**1**	**2**	**3**	**4**	**5**	**6**	**7**	**8**	**9**
Size (mm)	0.2-0.3	0.3-0.4	0.4-0.5	0.5-0.6	0.6-0.7	0.7-0.8	0.8-0.9	0.9-1.0	> 1.0

To validate the result, total air content calculated as the mean value and compared with ASTM C 457. With only 0.21% error, the air void measurement results from this approach were in very good agreement with the amount measured using ASTM C 457.

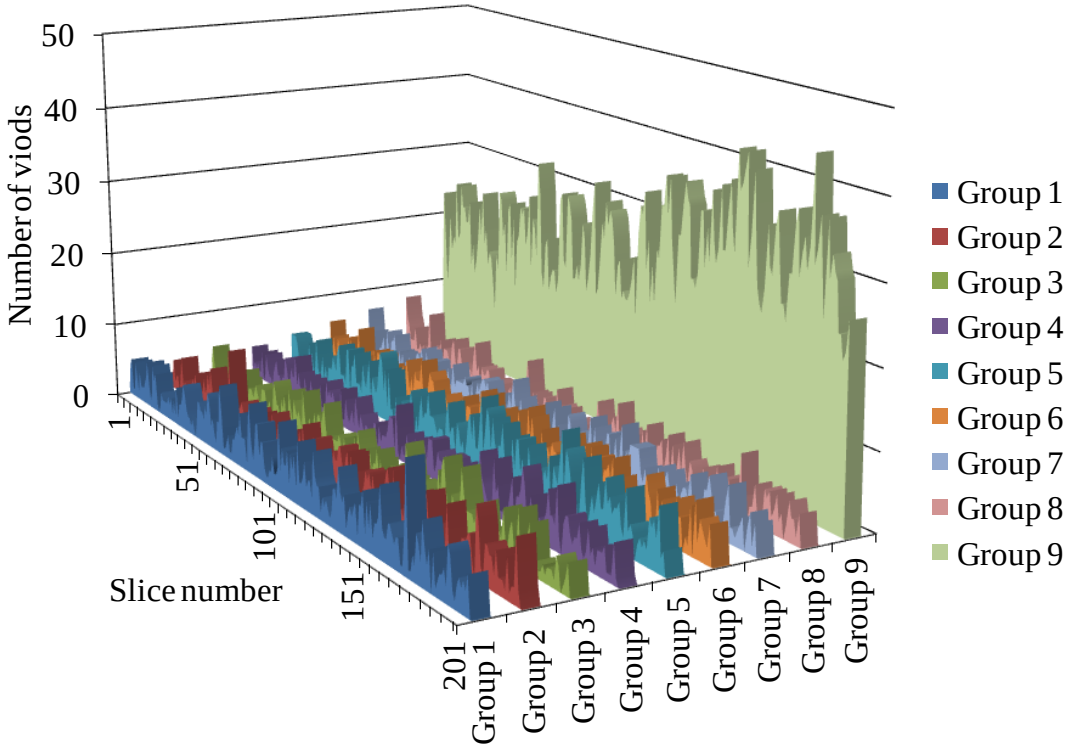

Figure. 4.1.1 Void distribution with their size and dimension groups

4.2. Coarse aggregate measurement

The amount of coarse aggregates was calculated for each section of QCT images as the ratio of the aggregates' area to the total section area. Figure 4.2.1 shows the aggregate distribution diagram. The mean volume fraction of coarse aggregate was calculated and compared with the amount in the mix design. The results show less than 1 % difference.

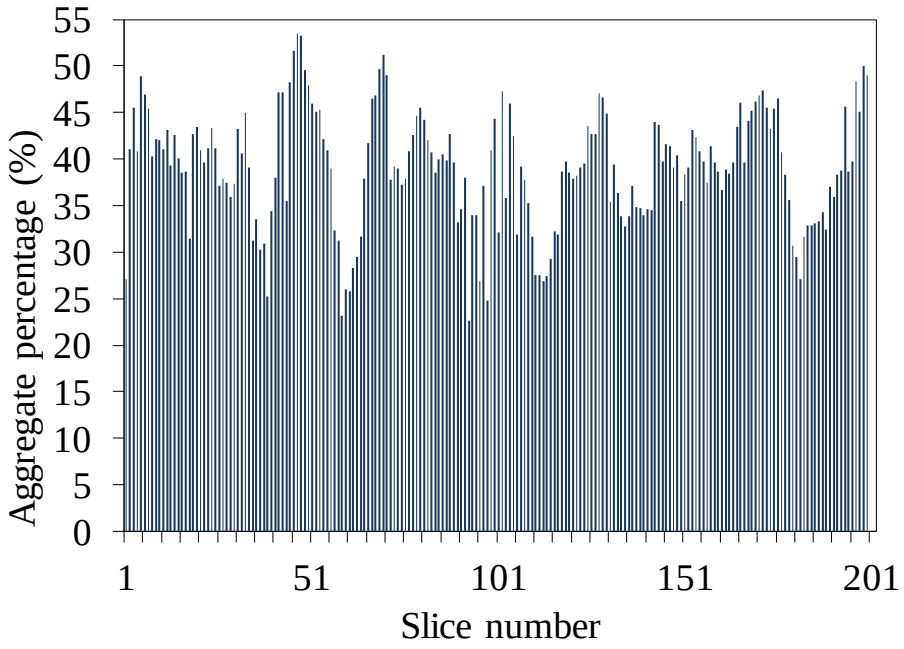

Figure. 4.2.1 Aggregate distribution diagram

4.3. Chloride diffusion

Fine and coarse aggregates can change the chloride diffusion in the concrete because of: (i) creating solid obstacles causing chloride ions move around them, and (ii) formation of ITZ around them which facilitates diffusion. The combination of these two opposite effects will define the overall transport properties of the concrete. In order to study the penetration of chloride ions into a concrete sample and validating the FEM results, five 100 mm x 100 mm concrete cylinders were cast and a reservoir created on the top of the each cylinder with aluminum tape.

The reservoirs were filled with 3% NaCl solution, as shown in Figure 4.3.1. Each month, one cylinder was split and the exposed surface was sprayed with 0.1 N silver-nitrate solution (Otsuki et al. 1992). After 24 hours, the diffused chloride ions in the concrete turned to a purple color,

and the depth of penetration was recorded. Measurements were carried out at three different locations on the sprayed surface and the average was used as the penetration depth. The minimum detectable chloride concentration in this method is 0.1% (Otsuki et al. 1992).

Figure 4.3.1. A sample with chloride solution ponding placed on the top of it

The finite element model that was created from the real concrete sample (section 3.3.3) similar to the abovementioned cylinders was used to model the chloride diffusion. Figure 4.3.2 shows the diffusion distribution obtained from the model. The average depth of penetration over time was calculated along three positions shown in Figure 4.3.3: lines A, B, and C, similar to the experimental procedure.

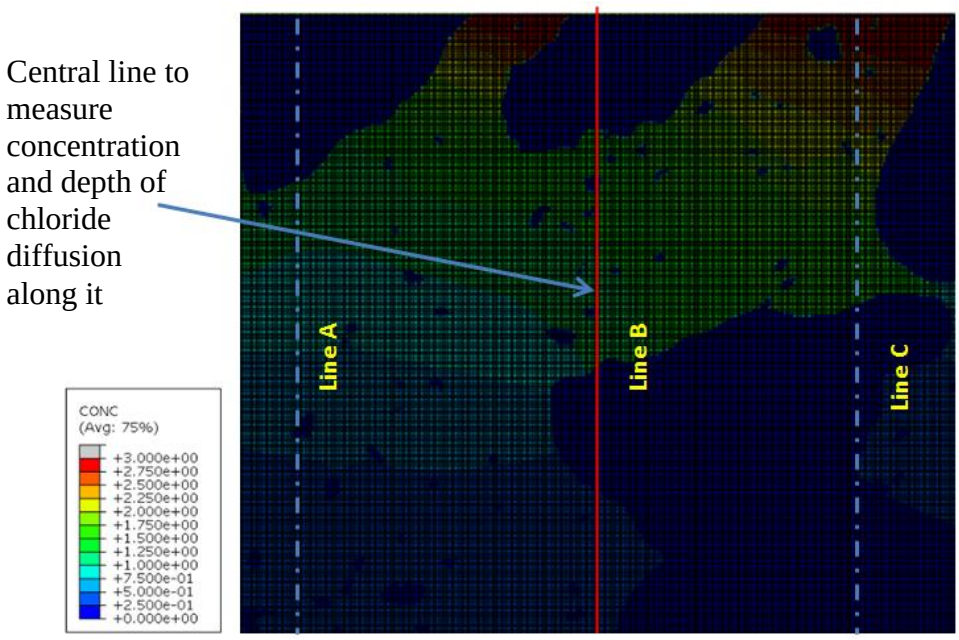

Figure. 4.3.2. Chloride diffusion contour

Figure 4.3.3 shows the concentration vs. time diagram for three states: without ITZ, ITZ considered only around coarse aggregates, ITZ considered around both coarse and fine aggregates. Since the diffusion into aggregates is negligible, interruptions appeared in diagrams. As can be seen, ITZ plays an important role in diffusion of chloride ions into concrete and it is imperative to consider it not only around coarse aggregates, but also around fine aggregates in the model.

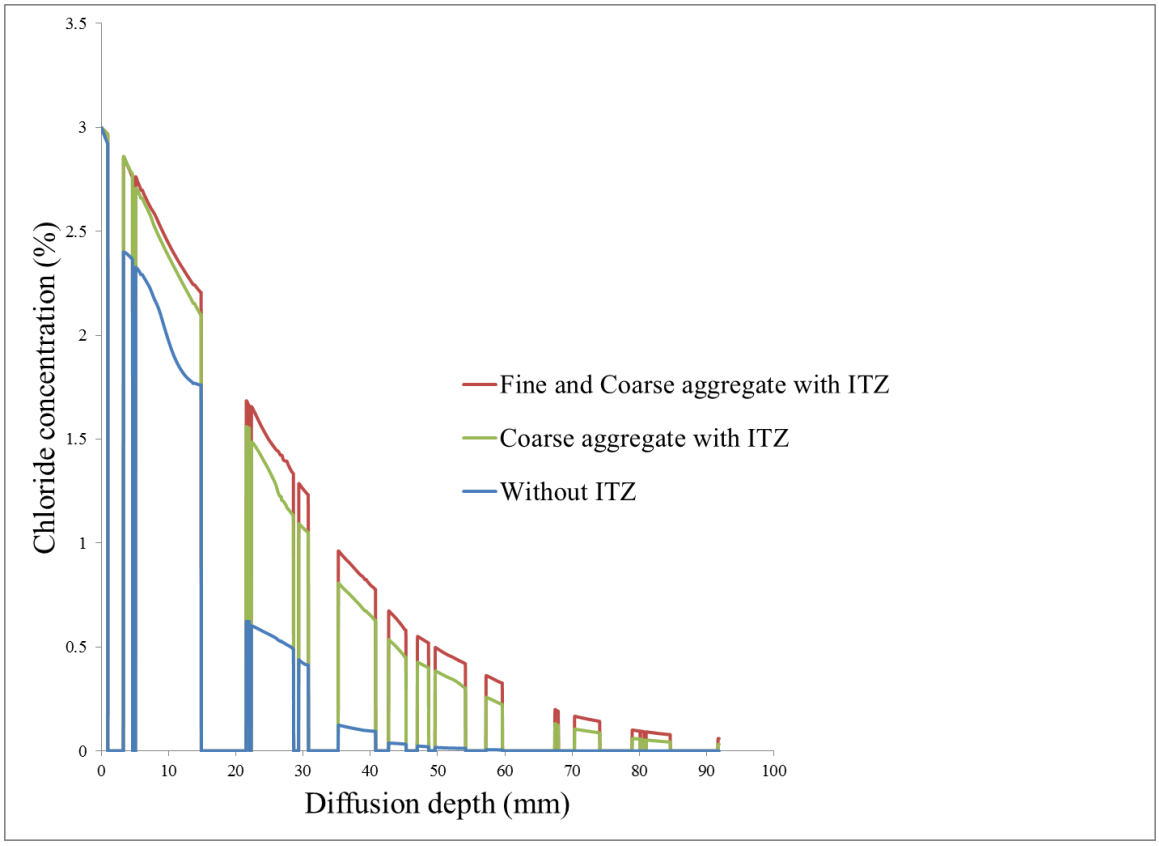

Figure. 4.3.3. Chloride diffusion vs. distance along central line for model with ITZ and without ITZ, 7000 hours after exposure to chloride ions

Figure 4.3.4 shows the error in concentration vs. depth diagram for three states: without ITZ and ITZ considered only around coarse aggregates with respect to amount calculated from ITZ considered around both coarse and fine aggregates. As it showed at the outer surface of concrete, the amount of error is zero for both situations by increasing a depth of penetration this error difference becomes greater in the situation without ITZ and after the depth of 40 mm it becomes constant in the upper bound of 90%, but this amount in the case with coarse aggregates considering ITZ increased linearly. As the typical cover depth in most concrete structures is around 4 inches, this thickness has been considered in diffusion analysis to compare with real condition.

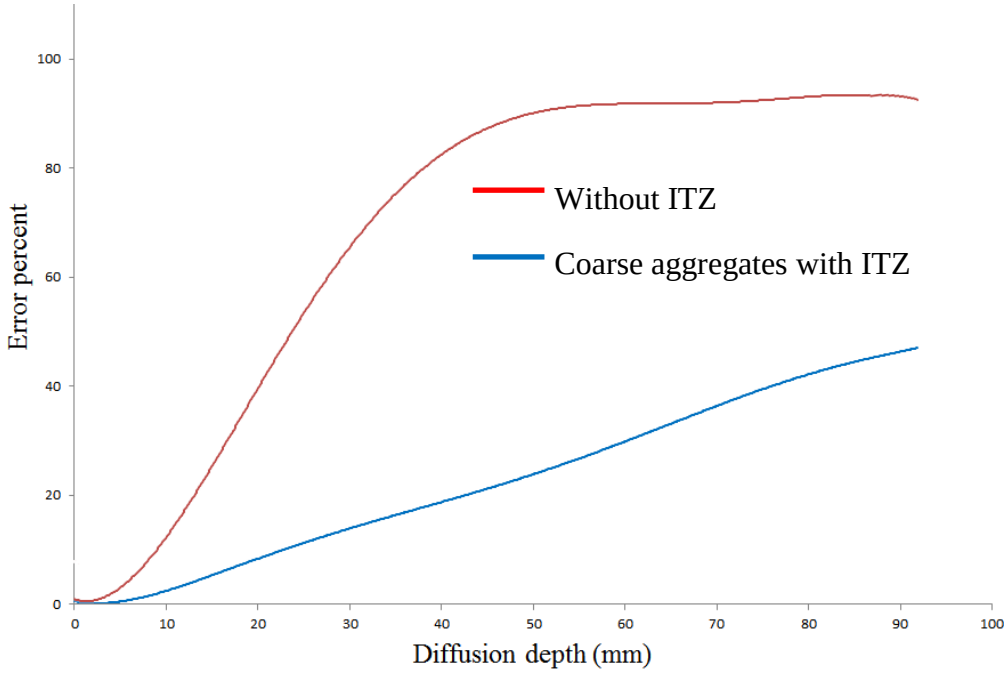

Figure. 4.3.4. Error induced from not considering ITZ in chloride diffusion

Figure 4.3.5 (a) shows the surface of one of the concrete cylinders, five months after exposure to NaCl, sprayed with $AgNO_3$ and Figure 4.3.5 (b) shows the model after the same period of time. As can be seen, the penetration profile and depth are very similar.

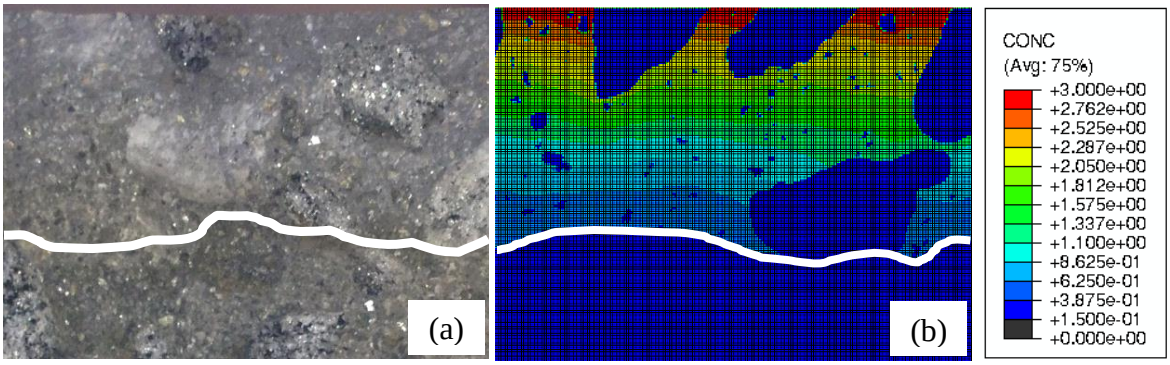

Figure. 4.3.5. Chloride penetration after one month (a) in an actual concrete sample and (b) predicted by finite element analysis

The average depth of penetration over time obtained from the experiment and the results from the FEM are shown together in Figure 4.3.5. as can be seen, a good agreement exists between the results from the FEM and those obtained from the experiments.

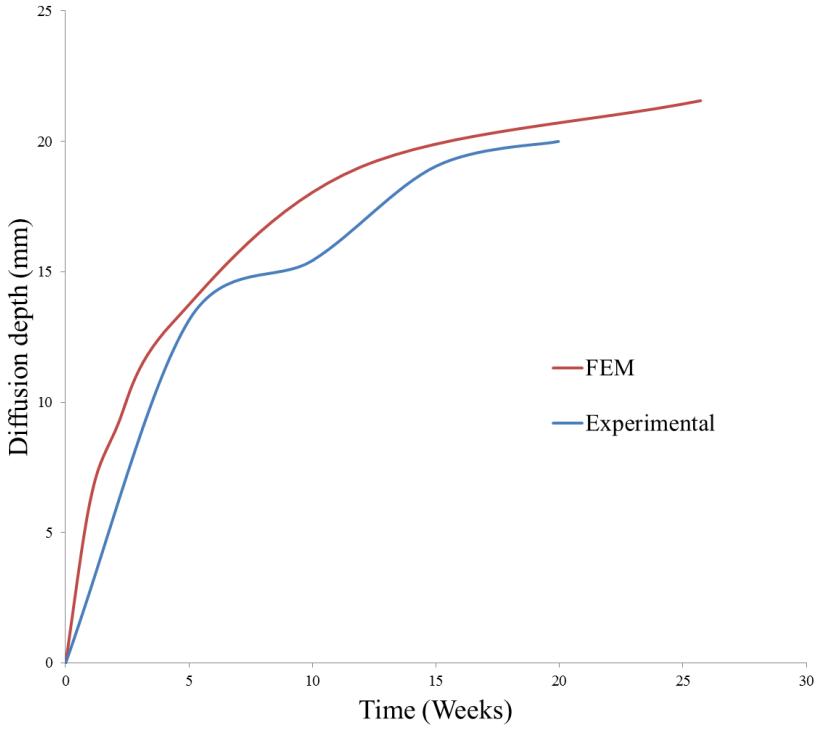

Figure 4.3.5. Comparing diffusion vs. time for both experimental and FEM results

4.4. The effect of aggregate distance to the reinforcing steel bar on chloride diffusivity

During the finite element analysis of chloride diffusion in concrete samples it was observed that the distance between coarse aggregates can affect the concentration of chloride ions in that region. As can be seen in Figure 4.3.6, the chloride concentration between two close coarse aggregates, in the region showed by the yellow circle, is higher than other locations at the same level in the model. It is well-known that chloride ions with a certain concentration (threshold) cause corrosion in steel in concrete. However, corrosion of steel in an actual concrete environment initiates with no predictable pattern.

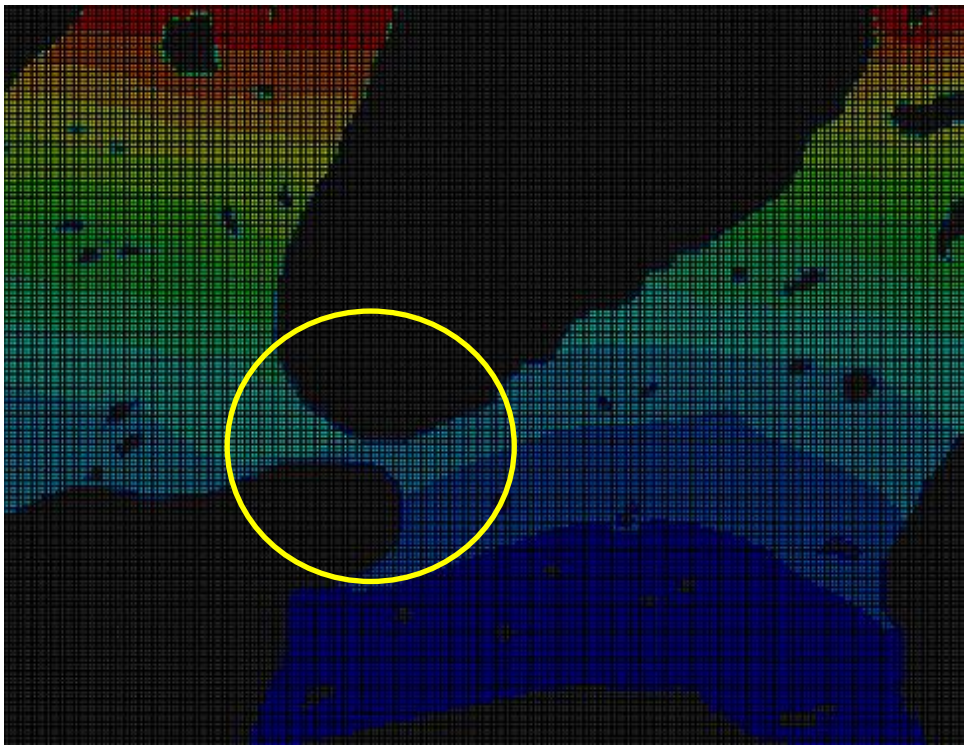

Figure 4.3.6. Effect of aggregates distance on chloride concentration and diffusion

On the other hand, due to time consumption of performing the required tests in studying corrosion of steel in a concrete environment, researchers, tend to use pore solution, cement paste or mortar instead of actual concrete to accelerate the chloride diffusion and facilitate corrosion. Valuable information can be obtained from these studies. However, the random initiation of corrosion in an actual concrete environment compared to that in pore solution, paste or mortar has always been a question and concern. It seemed the abovementioned observation might be one of the reasons for the unpredictability of corrosion initiation on the surface of steel.

To confirm this hypothesis with regard to the observation from the FEM analysis, three paste samples, with water-to-cement of 0.5 were cast. Each sample contained three aggregates and

three pieces of steel bar. Aggregates were located with different distances (3mm, 5mm and 10mm) to the surface of the steel bars. The three aggregates were manufactured from a large piece of stone. As shown in Figure 4.4.1, the stone was cut into smaller pieces and then the tip of each piece was ground.

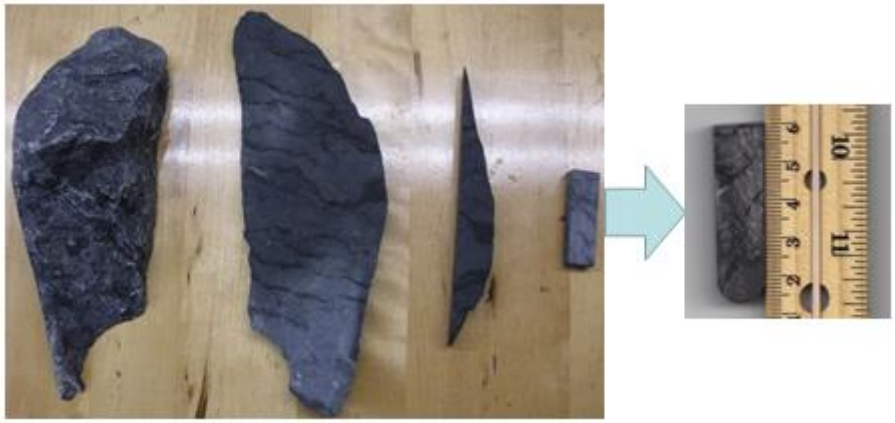

Figure 4.4.1. Process of cutting a round shape from chunk of limestone aggregate

The dimensions of the manufactured aggregates and their positions with respect to the steel bar are shown in Figure 4.4.2. To prepare each sample, 40mm pieces were cut from a #4 low carbon steel bar. The surface of each piece was cleaned with a wire brush prior casting. A hole was drilled at one end of each piece for electrical connection and then both sides (10mm from each side) of each piece was epoxy coated to prevent extraneous effect and to define the exposed length of 20mm. Two O-rings were used for each steel piece to hold the steel in the required position in the mold. The O-rings were glued to the mold.

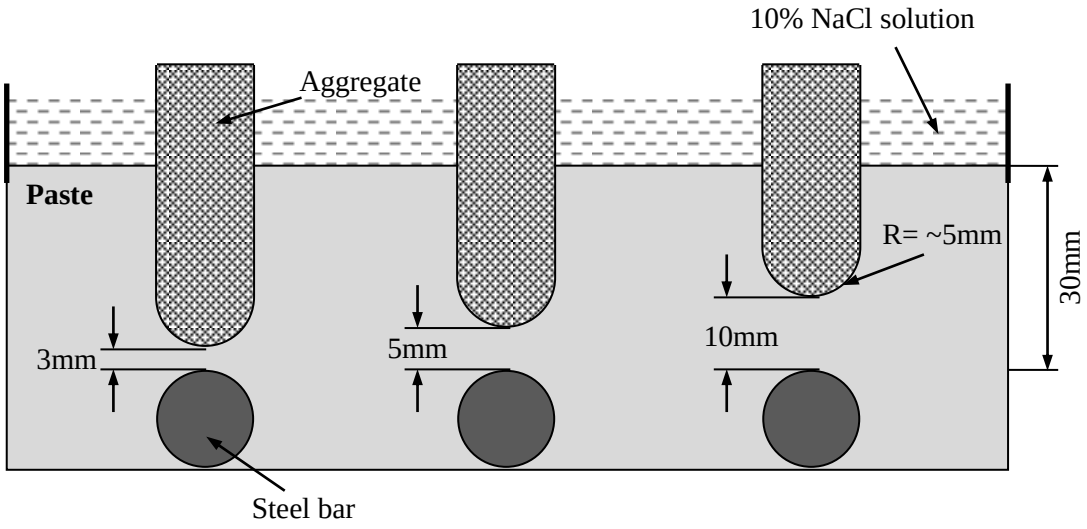

Figure 4.4.2. Schematic illustration of one of the paste samples with aggregates in different positions with respect to steel bar

This design allowed the paste to cover the whole bare surface of the steel with paste which was required for complete passivation. Figure 4.4.3 shows a mold with the steel pieces before casting. After casting, each sample was covered with a wet towel and plastic sheet. 24 hours after casting, the samples were demolded and wet cured for another 24 hours. Figure 4.4.4 shows one of the samples

Figure 4.4.3 Position of steel bars at the bottom of the mold

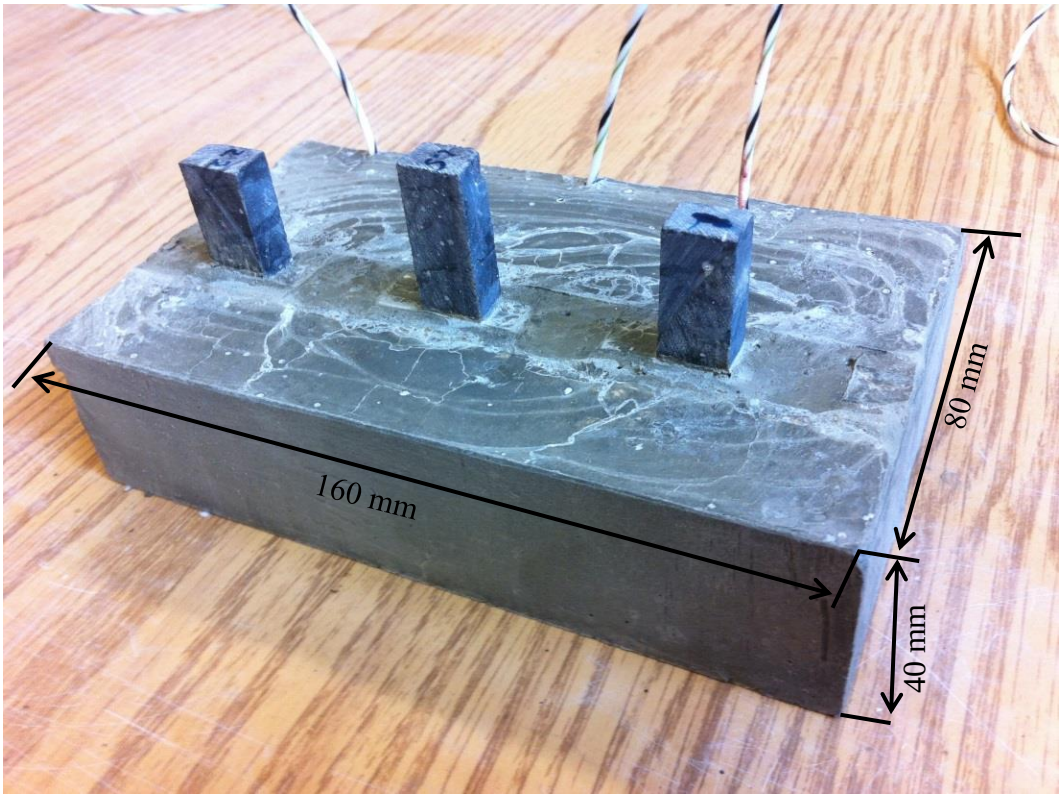

Figure 4.4.4. One of the samples after demolding

A reservoir was then made on the top of the each sample with aluminum tape. One week after casting, the reservoir on each sample was filled with 10% NaCl solution. Corrosion activity of each steel bars was measured using half-cell potential, LPR and cyclic polarization techniques. A 2D FEM model was also created in ABAQUS, as shown in Figure 4.4.5.

The model considered three aggregates in different positions, with respect to the bottom of the model and the ITZ around each aggregate had a thickness of 40 μm. Mesh was assigned to the model by using 2773 nodes and 2605 elements including quadrilateral and triangular.

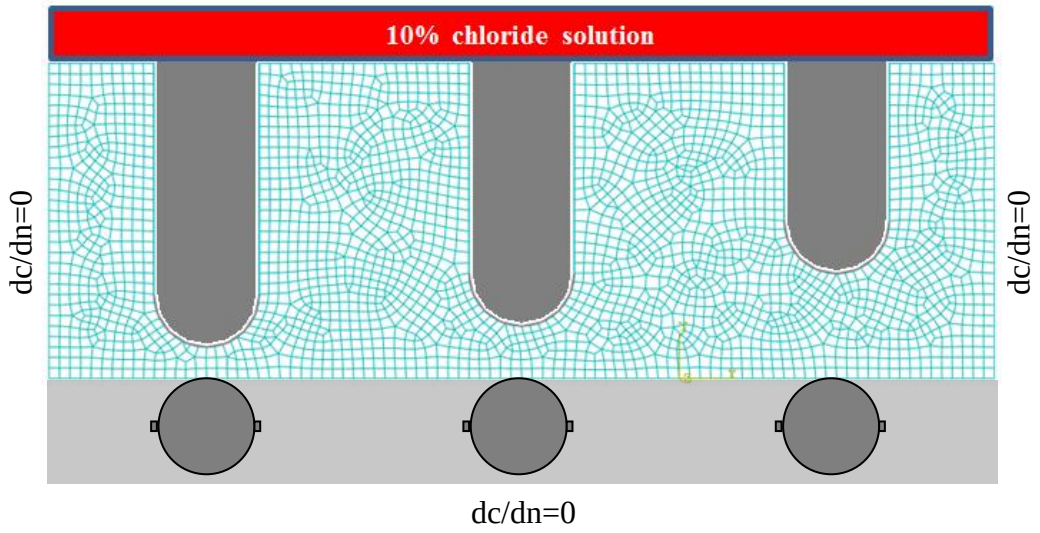

Figure 4.4.5 Finite element model of the paste samples with aggregates in different positions

A 10% NaCl solution was applied on the top surface of the model and the boundary condition with zero gradient of concentration on all other surfaces. The results obtained from the FEM analysis after 3, 4 and 5 months are shown in Figure. 4.4.6. to 4.4.8, respectively. The comparison between the contours in Figures 4.4.6, 4.4.7 and 4.4.8 exhibit the profound difference of the chloride diffusion process due to the variation of distance between aggregates and the bottom of the model which represents steel bars.

As can be seen in Figure 4.4.6 (a), the chloride concentration reached the typical threshold value mentioned by ACI 222R-12 for steel in concrete for the steel piece with 3mm distance from the aggregate before the other two bars in 12 weeks.

After 16 weeks as Figure 4.4.7 (b) shows chloride ions with chloride threshold value reached to the surface of the steel bar with 5mm distance to the aggregate and finally after 20 weeks chloride ions with the threshold concentration reached the surface of the steel bar with 10 mm distance to the aggregate, as illustrated in Figure 4.4.8 (c).

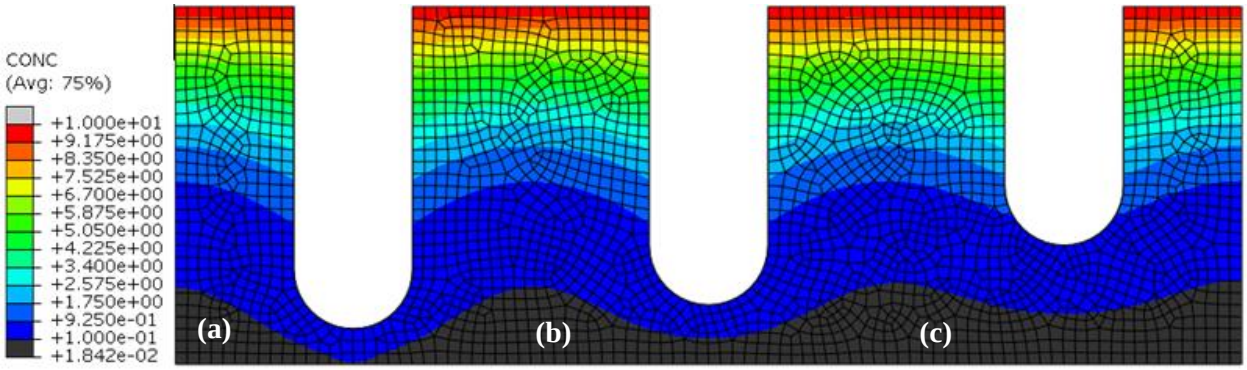

Figure 4.4.6. Comparing the chloride diffusion in three different distances of aggregate to the steel bar;12 weeks is the required time for chloride ions to reach their threshold value at the surface of the steel bar with 3mm distance to the aggregate (a)

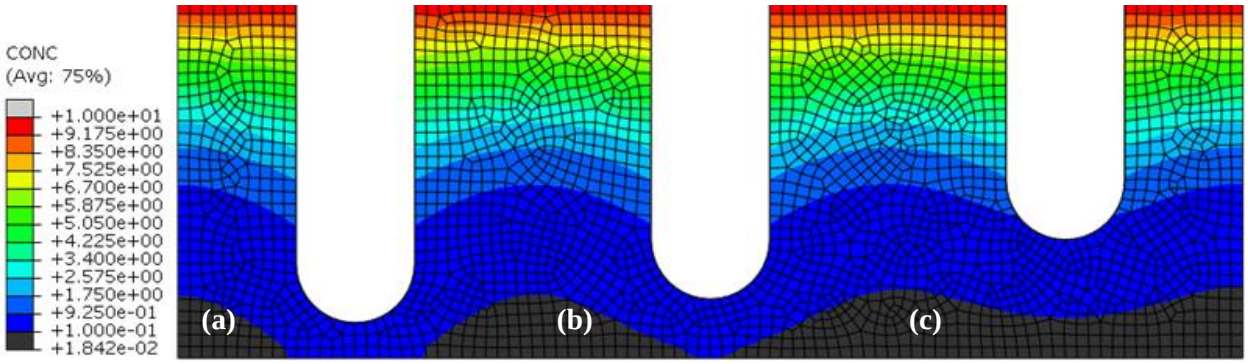

Figure 4.4.7. Comparing the chloride diffusion in three different distances of aggregate to the steel bar; 16 weeks is the required time for chloride ions to reach their threshold value at the surface of the steel bar with 5mm distance to the aggregate (b)

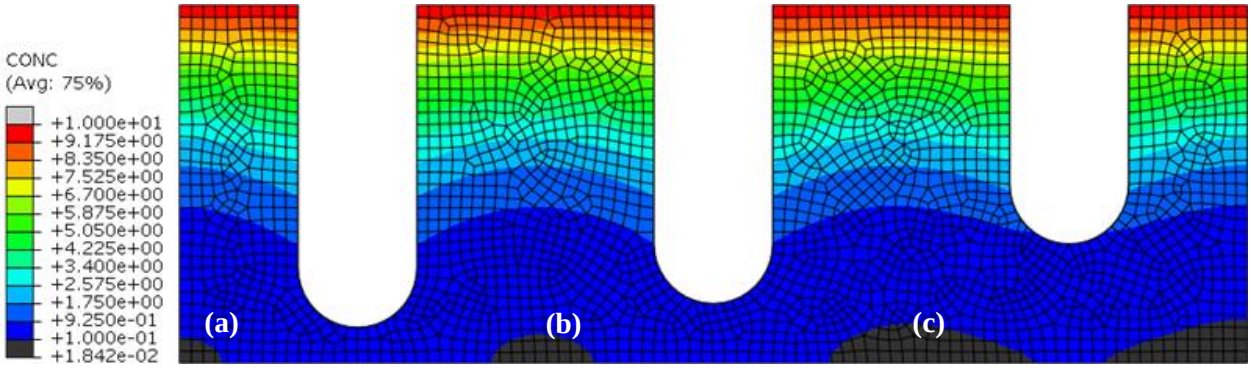

Figure 4.4.8. Comparing the chloride diffusion in three different distances of aggregate to the steel bar; 20 weeks is the required time for chloride ions to reach their threshold value at the surface of the steel bar with 10mm distance to the aggregate (c)

The half-cell potential values of each bar of the steel bars in each sample (Figure 4.4.9.) were measured versus the saturate Calomel reference electrode. The potential of the steel bars were more positive then -150mV versus Calomel electrode for about 11 weeks indicating passive state. The LPR was also performed during this period and corrosion current densities of the bars were calculated.

All values were around 10^{-3} $A.m^{-2}$, which confirmed the results of the half-cell potential measurements. 11 weeks after exposure to NaCl solution, both half-cell potential and LPR tests confirmed occurrence of corrosion on the steel bar with 3mm distance from the aggregate.

The cyclic polarization test was also carried after 11 weeks of exposure to NaCl to confirm the results of the half-cell potential and the LPR tests. As can be seen in Figure 4.4.9, results from the cyclic polarization test clearly shows corrosion on the surface of the bar with 3mm distance from the aggregate.

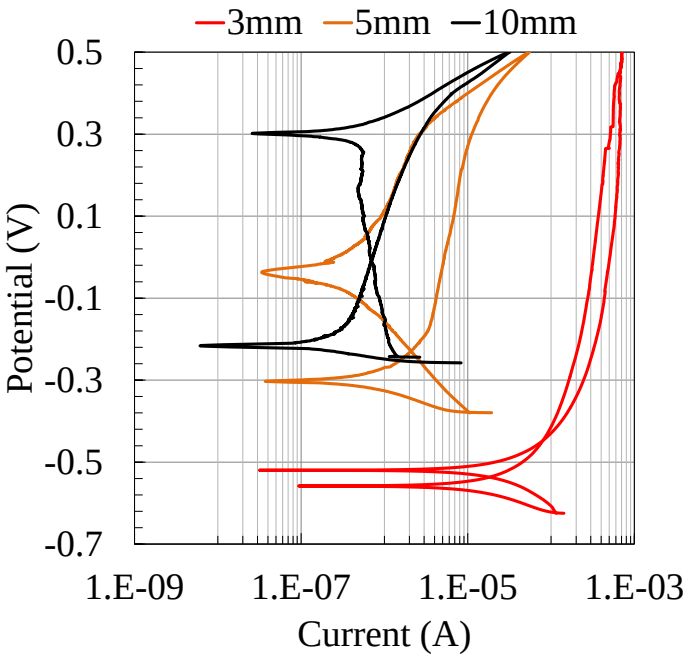

Figure 4.4.9. Results from cyclic polarization test on the steel bars with different distances from aggregate, 11 weeks after exposure to 10% NaCl

To confirm the results from the electrochemical measurements, one of the samples was autopsied. As shown in Figure 4.4.10, the surface of the bar with 3mm distance from the aggregate clearly shows corrosion on it the after 11 weeks while the other pieces were intact.

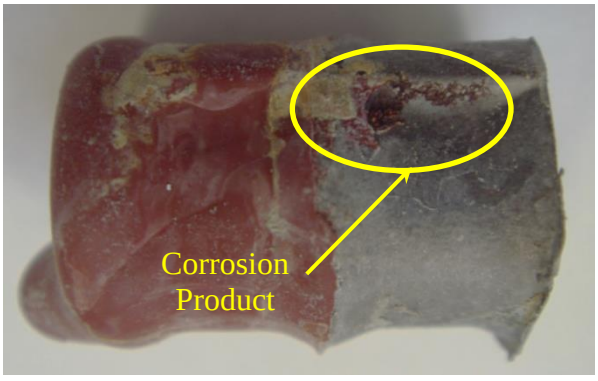

Figure 4.4.10. Corrosion on the surface of the steel bar with 3mm distance to the aggregate

These experimental results clearly confirmed the results obtained from the model. Both results indicate the significance of the presence and the location of coarse aggregates versus the steel bars in studying the corrosion of steel in concrete due to chloride attack. Approximately 15.5 and 19 weeks after exposure to 10% NaCl, the corrosion was initiated on the steel bars with 5mm and 10mm distances to the aggregates, respectively; confirming the results from FEM analysis.

4.5. The effect of aggregate shape on chloride diffusivity

The effect of aggregate shape on chloride diffusion was modeled by considering five different shapes of aggregates including; circular aggregate, octagonal aggregate, hexagonal aggregate, pentagonal aggregate and quadrilateral aggregate and casted in cement paste.

Two different scenarios were considered for analysis; in both cases the ITZ was included. The first scenario was the case that each aggregate has inscribed in a circle which has a diameter of 5 mm. ITZ with the thickness of 40 μm was also included around each aggregate. This case was selected to represent the aggregates passing through a 5 mm sieve. In this case, each aggregate has different surface area compare to that on other aggregates. The second scenario was the case that aggregates have equal perimeters and an ITZ with 40 μm thickness also included around each aggregate. In this case, all aggregates have similar ITZ areas.

Mesh was assigned to the models using quadrilateral and triangular elements. A 3% NaCl solution was applied as the boundary condition on the top surface of the model and the boundary conditions with zero gradient of concentration were considered on all other surfaces.

The results obtained from the FEM analysis for the first case after four weeks are shown in Figures 4.5.1. and 4.5.2. The comparison between the contours in Figure 4.5.1, (a) to (e) exhibit the difference of the chloride diffusion process due to the variation of aggregate shapes. As Figure 4.5.2 shows, quadrilateral aggregate has the highest concentration of chloride and hexagonal aggregate has the lowest among all.

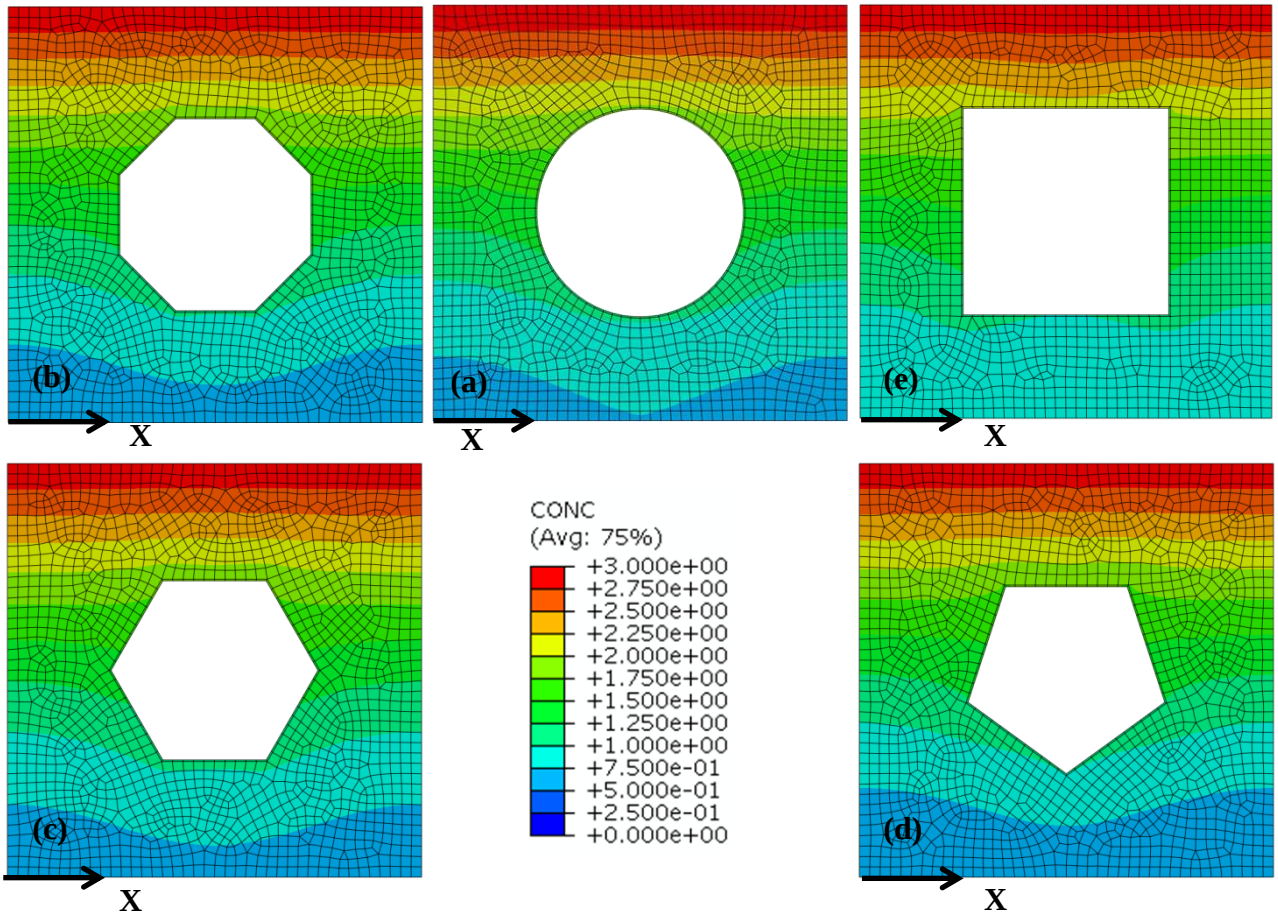

Figure 4.5.1. five different shapes of aggregate inscribed in a circle with diameter 5 mm, (a) circular aggregate, (b)octagonal aggregate, (c) hexagonal aggregate, (d) pentagonal aggregate, (e) quadrilateral aggregate

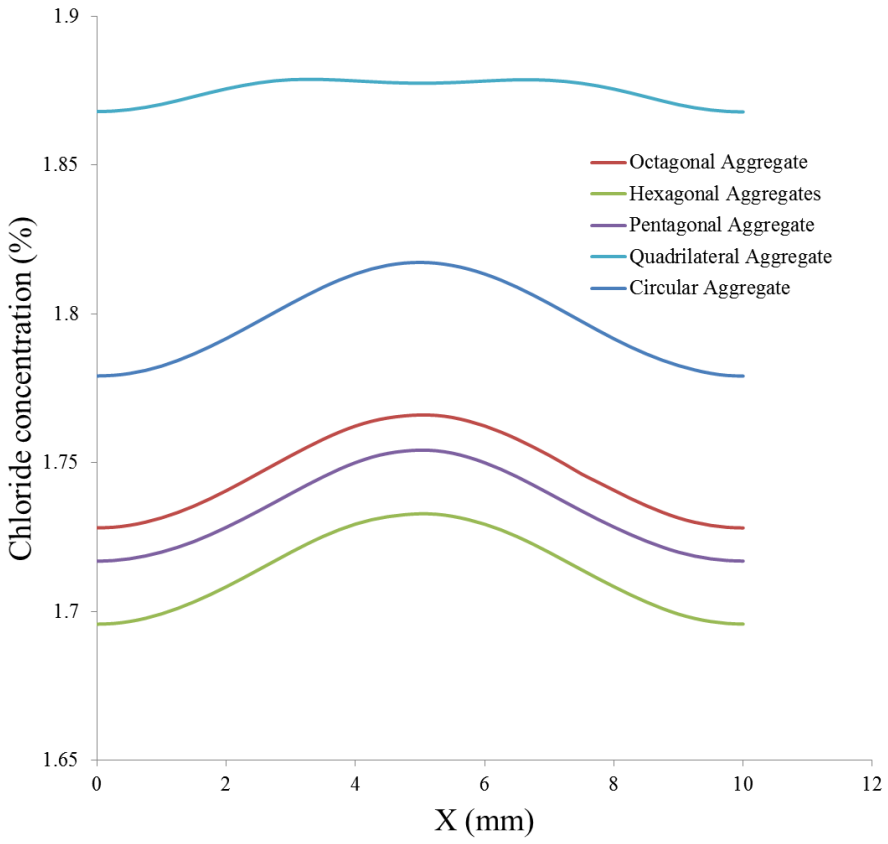

Figure 4.5.2.Concentration profiles along the horizontal line at the bottom of the model for different shape of aggregate with equal size

The results obtained from the FEM analysis for different shape of aggregates with equal ITZ size after four weeks are shown in Figure. 4.5.3. and 4.5.4. As can be seen, quadrilateral aggregate has the lowest concentration of chloride and circular aggregate has the highest among all.

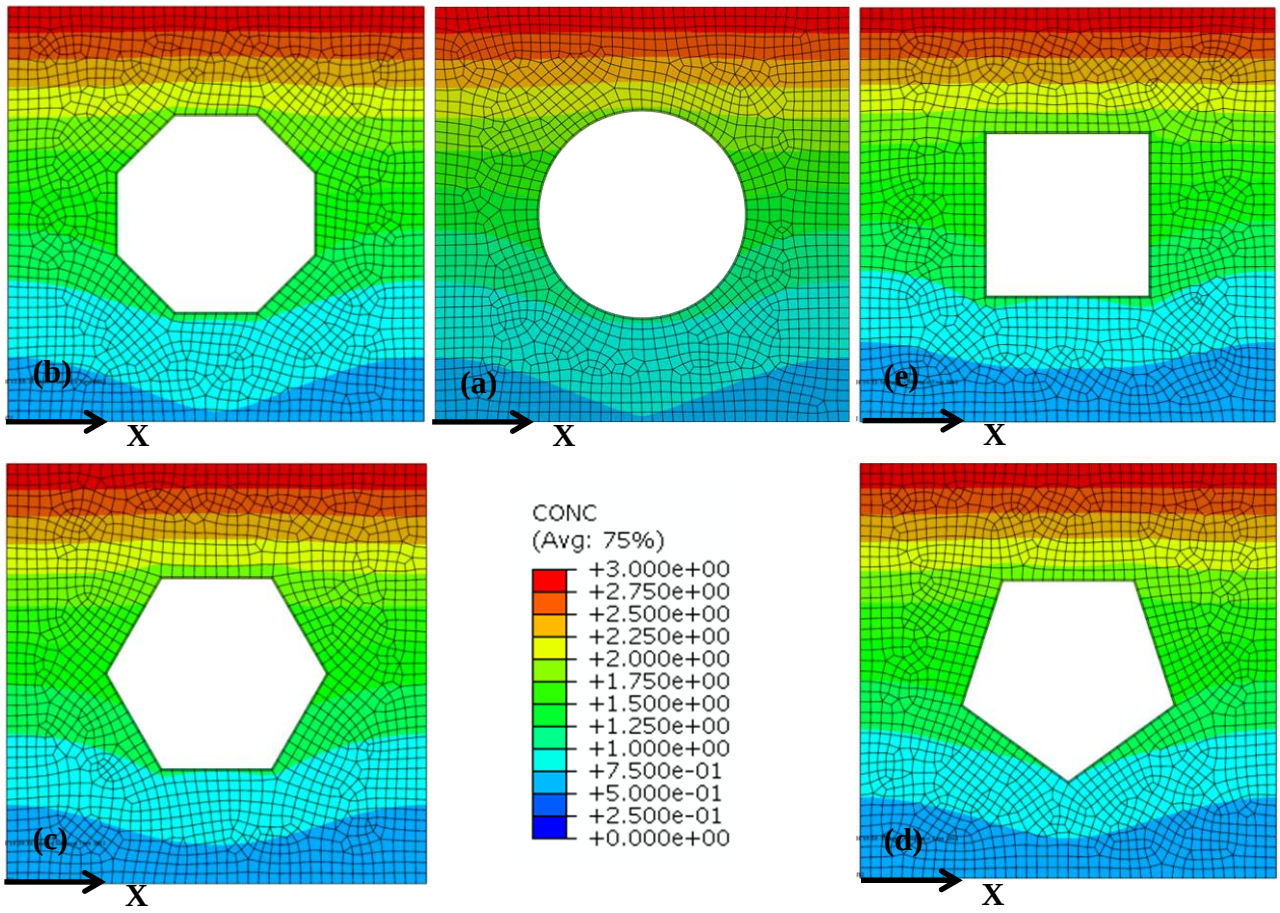

Figure 4.5.3. five different shapes of aggregate equivalent with perimeter of a circle with diameter 5 mm, (a) circular aggregate, (b)octagonal aggregate, (c) hexagonal aggregate, (d) pentagonal aggregate, (e) quadrilateral aggregate

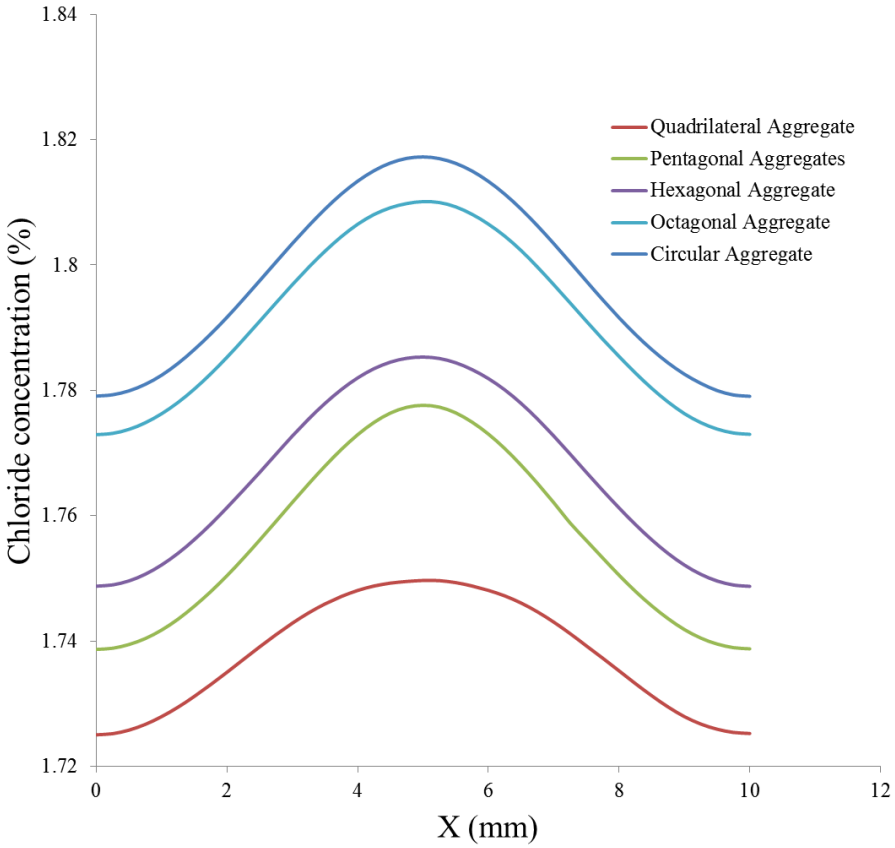

Figure 4.5.4. Concentration profiles along the horizontal line at the bottom of the model for different shape of aggregate with equal ITZ size

CHAPTER 5: SUMMARY OF THE RESULTS, CONCLUSIONS AND FUTURE WORKS

5.1. Summary and conclusions

- QCT along with image analysis techniques was successfully used to study the air void content and distribution as well as coarse aggregate content in concrete in 3D. A good agreement between the results from this method and those from the microscopic analysis was observed. The major advantage of QCT technique is much short time required for analysis with the QCT method compared to that with the conventional microscopic studies . In addition, information in 3D can be obtained using the QCT images.
- In the study of chloride diffusion in concrete, it is imperative to consider the actual shape of aggregates as well as ITZ around both fine and coarse aggregates. The chloride concentration gradient when ITZ is considered around aggregates is much higher compared to that in concrete without considering the ITZ. The position of coarse aggregates can also effect on the diffusion process and the chloride ion diffusivity. The experimental and simulation results indicate that closer aggregates to the steel bar can increase the rate of the chloride diffusion as well as the rate of corrosion.

5.2. Future works and suggestions

The following activity is suggested for future works:

- The effect of aggregate distribution and size on chloride diffusion needs to be studied, experimentally and by using FEM approach developed in this research. If available, a CT scanner with higher resolution should be used to obtain images with higher quality. This approach might resolve the issue with fine aggregate detection.
- If constructing a 3D image containing fine aggregates is successful, then a 3D FE model should be prepared and chloride diffusion should be studied in 3D.
- In 3D FEM, one of the issues is the number of elements and nodes in the model with forces using a super computer. Another approach for reducing the number of nodes and elements, without jeopardizing the analysis needs to be studied.
- In this study, the 2D model was created with different manual steps. These steps (except the polishing step) need to be automated to minimize the time and operator dependency.
- Large slabs should be made and modeled. The natural corrosion due to chlorides should then be studied with both experimental and modeling approaches. This is required to further confirm the modeling procedure in this study.

Appendix A: 3D Concrete finite element model

Figure A1. Concrete 3D finite element model

Figure A2. Sectioned view of concrete 3D finite element model (Fine mesh 0.5x0.5x1mm^3)

Figure A3. Sectioned view of concrete 3D finite element model (Coarse mesh 1x1x1mm^3)

Appendix B: Cross section of the samples exposed to chloride diffusion detected with AgNO3 solution

Figure B.1. Chloride penetration after one month

Figure B.2. Chloride penetration after two month

Figure B.3. Chloride penetration after three month

Figure B.4. Chloride penetration after four month

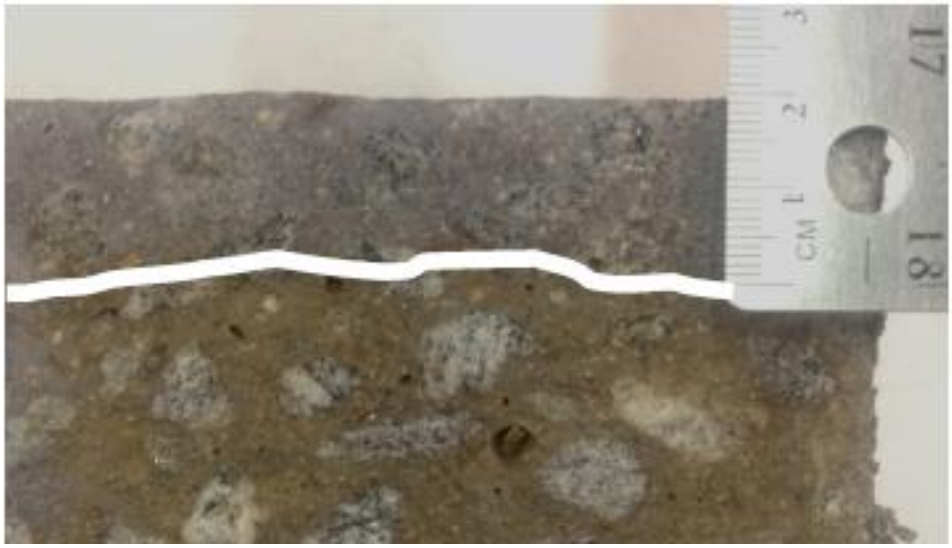

Figure B.5. Chloride penetration after five month

Appendix C: Experimental setup to study the effect of aggregate distance on corrosion initiation

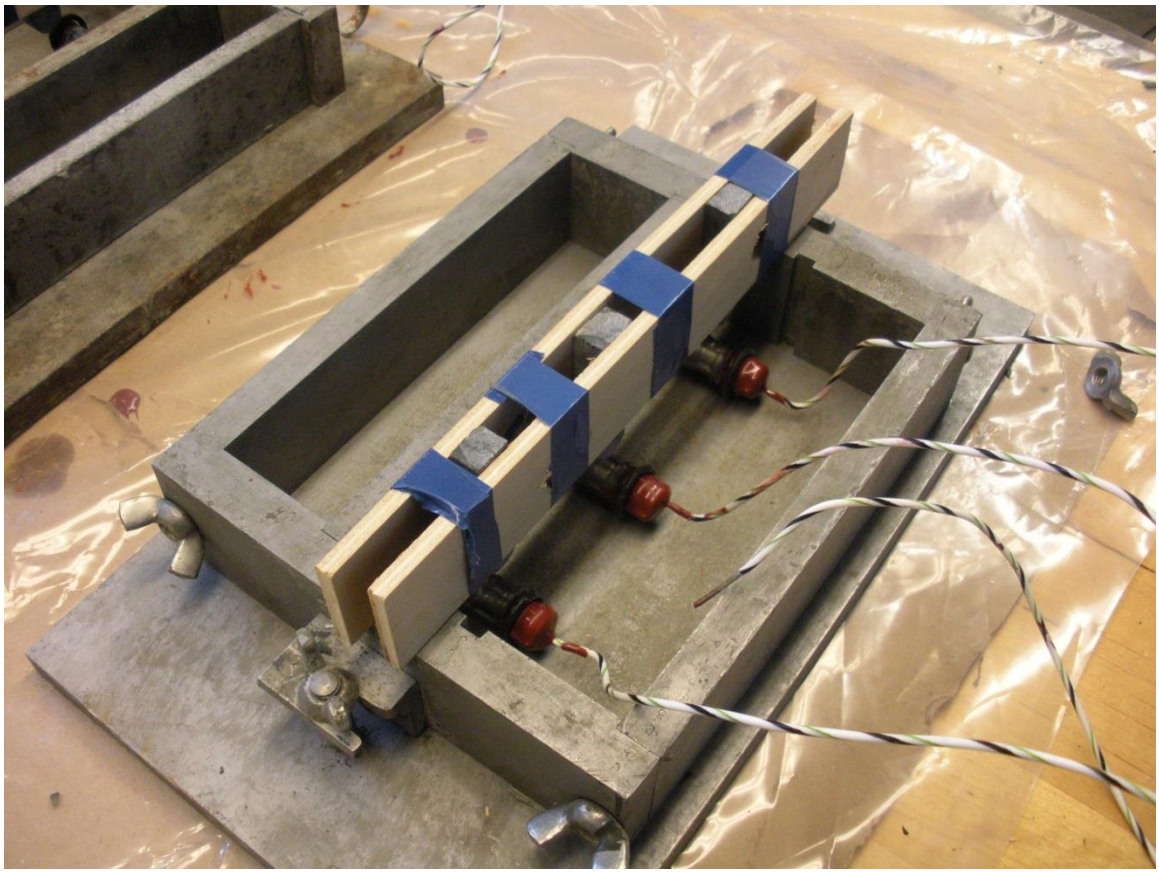

Figure C.1. Fixture to remain three in desire distance

Figure C.2. Sample with chloride reservoir of top of it

REFERENCES

Abdel-Qader, I., O. Abudayyeh and M. E. Kelly (2003). "Analysis of Edge-Detection Techniques for Crack Identification in Bridges." Computing in Civil Engineering 17(4): 255-263.

ACI Committee 222 (1996). 222R-96: Corrosion of Metals in Concrete.

Ahmed, S. (2003). "Reinforcement corrosion in concrete structure, its monitoring and service life prediction-a review." Cement and Concrete Composite 30(4-5): 459-471.

Andrade, C. and J. A. González (1978). "Quantitative measurements of corrosion rate of reinforcing steels embedded in concrete using polarization resistance measurements." Werkstoffe und Korrosion 29: 515-519.

Andrade, C., A. Marcias, S. Feliu, M. L. Escudero and J. A. Gonzalez (1990). Quantitative measurement of the corrosion rate using a small counter electrode in the boundary of passive and corroded zones of a long concrete beam. Corrosion Rates of Steel in Concrete, ASTM STP 1065. N. S. Berke, V. Chaker and D. Whiting. Philadelphia, PA, ASTM.

Apostolopoulosa, C. A., S. Demisb and V. G. Papadakisc (2013). "Chloride-induced corrosion of steel reinforcement – Mechanical performance and pit depth analysis." Construction and Building Materials 38: 139-146.

Askeland, D. R. and P. P. Phule (2003). The science and engineering of materials.

ASTM (1998). "G 61-86: Standard Test Method for Conducting Cyclic Potentiodynamic Polarization Measurements for Localized Corrosion Susceptibility Iron, Nickel, or Cobalt-Based Alloys." 03.02.

ASTM (1999). "C876-91: Standard Test Method for Half-cell Potentials of Uncoated Reinforcing Steel in Concrete." 03.02: 446-451.

ASTM (1999). "G 5-94: Standard Reference Test Method for Making Potentiostatic and Potentiodynamic Anodic Polarization Measurements." 03.02.

ASTM (2011). "C457: Standard Test Method for Microscopical Determination of Parameters of the Air-Void System in Hardened Concrete." 04.02.

Aydilek, A. H. and M. Guler (2003). "Use of Image Analysis in Determination of Strain Distribution in Geosynthetic Tensile Testing." Computing in Civil Engineering 18(1): 65-74.

Aydilek, A. H., S. H. Oguz and T. B. Edil (2002). "Digital Image Analysis to Determine Pore Opening Size Distribution of Nonwoven Geotextiles." Computing in Civil Engineering 16(4): 280-290.

Basheer, L., P. A. M. Basheer and A. E. Long (2005). "Influence of coarse aggregate on the permeation, durability and the microstructure characteristics of ordinary Portland cement concrete." Construction and Building Materials 19(9): 682-690.

Bentz, D. P., E. J. Garboczi and E. S. Lagergren (1998). "Multi-scale microstructural modeling of concrete diffusivity: Identification of significant variables." Cement Concrete and Aggregates 20(1): 129-139.

Bentz, D. P., J. T. G. Hwang, C. Hagwood, E. J. Garboczi, K. A. Snyder, N. Buenfeld and K. L. Scrivener (1994). "Interfacial zone percolation in concrete: effects of interfacial zone thickness and aggregate shape." Materials Resaerch Society.

Bentz, D. P., E. Schlangen and E. J. Garboczi (1995). "Computer simulation of interfacial zone microstructure and its effect on the properties of cement-based composites." Materials science of concrete IV: 155-199.

Bernard, F., S. Kamali-Bernard and W. Prince (2008). "3D multi-scale modelling of mechanical behaviour of sound and leached mortar." Cement and Concrete Composites 34(8): 449-458.

Breton, D., J. P. Ollivier, G. Ballivy and J. C. Maso (1992). "Interfaces in Cementitious Composites." RILEM International Conference, Toulouse.

Buenfeld, N. R. and E. Okundi (1998). "Effect of Cement Content on Transport in Concrete." Magazine of Concrete Research 50(4): 339-351.

Carnot, A., I. Frateur, P. Marcus and B. Tribollet (2002). "Corrosion mechanisms of steel concrete moulds in the presence of a demoulding agent." Journal of Applied Electrochemistry 32: 865-869.

Chen, P. H., Y. C. C. L. M. Chang and P. C. Doerschuk (2002). "Application of Multi-resolution Pattern Classification to Steel Bridge Coating Assessment." Computing in Civil Engineering 16(4): 244-251.

Collepardi, M., A. Marcialis and R. Turriziani (1967). "Kinetics of penetration chloride ions in concrete." IL Cemento 4: 157-163.

Corbett, R. A. "Laboratory corrosion testing of medical implants." Corrosion Testing Laboratories, Inc., Newark, Delaware, USA, ASM International.

Corrosion-club (2004). http://www.corrosion-club.com/concretecorrosion.htm.

Corrosion-doctors (2005). http://www.corrosion-doctors.org.

Crank, J. (1979). "The mathematics of diffusion." Oxford university press.

Delagrave, A., J. P. Bigas, J. P. Ollivier, J. Marchand and M. Pigeon (1997). "Influence of the interfacial zone on the chloride diffusivity of mortars." Advanced Cement Based Materials 5(3-4): 86-92.

Elsener, B., C. Andrade, J. Gulikers, R. Polder and M. Raupach (2003). "Half-cell potential measurements – Potential mapping on reinforced concrete structures." Materials and Structures 36.

Elsharief, A., M. D. Cohen and J. Olek (2003). "Influence of aggregate size, water cement ratio and age on the microstructure of the interfacial transition zone." CEMENT and CONCRETE RESEARCH 23(11): 1837-1849.

Farran, J. (1956). Revue Des Materiaux De Construction.

FORCE Technology (2004). "Evolution of corrosion in reinforced concrete structures." www.force.dk/NR/rdonlyres/7A1681DB-71A2-4424-B948-D44EEDC38C35/204/17861en3.pdf.

Funahashi, M. (1990). "Predicting corrosion-free service life of a concrete structure in a chloride environment." ACI Materials Journal 87(6): 581-587.

Garboczi, E. J. (2002). "Three-dimensional mathematical analysis of particle shape using X-ray tomography and spherical harmonics: Application to aggregates used in concrete." Cement and Concrete Composites 32(10): 1621-1638.

Garboczi, E. J. and D. P. Bentz (1991). "Digital simulation of the aggregate-cement paste interfacial zone in concrete." Journal of materials Research 6(1): 196-201.

Garboczi, E. J. and D. P. Bentz (1996). "Modeling of the microstructure and transport properties of concrete." Construction and Building Materials 10(5): 293-300.

Garboczi, E. J., L. M. Schwartz and D. P. Bentz (1995). "Modeling the influence of the interfacial zone on the DC electrical conductivity of mortar." Advanced Cement Based Materials 2(5): 169-181.

Gjorv, O. E. and O. Vennesland (1979). "Diffusion of chloride ions from sea water into concrete." CEMENT and CONCRETE RESEARCH 9(2): 229-238.

Gonzalez, R. C. and R. E. Woods (2009). "Digital Image Processing." Gatesmark Publishing.

Hadley, D. W. (1972). "The Nature of The Paste-Aggregate Interface." West Lafayette, Purdue University. Ph.D. Thesis.

Hansson, C. M. (1984). "Comments on electrochemical measurements of the rate of corrosion of steel in concrete." Cement and Concrete Research 14: 574-584.

Hartman, A. M. and M. D. Gilchrist (2004). "Evaluating Four-Point Bend Fatigue of Asphalt Mix Using Image Analysis." Materials in Civil Engineering 16(1): 60-68.

Hoar, T. P. (1967). "The production and breakdown of the passivity of metals." Corrosion Science 7: 341-355.

Jahne, B. (2004). "Practical handbook on image processing for scientific and technical applications."

Jakobsen, U. H., C. Pade, N. Thaulow, D. Brown, S. Sahu, O. Magnusson, S. D. Buck and S. D. Schutter (2006). "Automated air void analysis of hardened concrete- a Round Robin study." CEMENT and CONCRETE RESEARCH 36(8): 1444-1452.

Jensen, O. M., P. F. Hansen, A. M. Coats and F. P. Glasser (1999). "Chloride ingress in cement paste and mortar." CEMENT and CONCRETE RESEARCH 29(9): 1497-1504.

Jones, D. A. (1992). "Principles and Prevention of Corrosion." Macmillan Publishing Company.

Kim, K. Y., T. S. Yun, J. Choo, D. H. Kang and H. S. Shin (2012). "Determination of air-void parameters of hardened cement-based materials using X-ray computed tomography." Construction and Building Materials 37: 93-101.

Koller, D., K. Daniilidis and H. H. Nagel (1993). "Model-Based Object Tracking in Monocular Image Sequences of Road Traffic Scenes." International Journal of Computer Vision 10(3): 257-281.

Lanzón, M., V. Cnudde, T. Kock and J. Dewanckele (2012). "X-ray microtomography (μ-CT) to evaluate microstructure of mortars containing low density additions." Cement and Concrete Composites 34(9): 993-1000.

Liam, K. C., S. K. Roy and D. O. N. wood (1992). "Chloride ingress measurements and corrosion potential mapping study of a 24-year-old reinforced concrete jetty structure in a tropical marine environment." Magazine of Concrete Research 44(160): 205-215.

Lin, D. F., H. Y. Wang and H. L. Luo (2004). "Assessment of Fire-Damaged Mortar Using Digital Image Process." Materials in Civil Engineering 16(4): 383-386.

Manahiloh, K. N., B. Muhunthan and M. Kayhanian (2012). "X-ray computed tomography and nondestructive evaluation of clogging in porous concrete field samples." Materials in Civil Engineering 24(8).

Marcotte, T. D. (2001). "Characterization of Chloride-Induced Corrosion Products that form in Steel-Reinforced Cementitious Materials." PhD thesis, University of Waterloo.

MATLAB (2012). Ver 7.14.0.739 (R2012a). Natick, Massachusetts, The MathWorks Inc.

Midgley, H. G. and J. M. Illston (1984). "The penetration of chlorides into hardened cement pastes." CEMENT and CONCRETE RESEARCH 14(4): 546-558.

Mindess, S., J. F. Young and D. Darwin (2003). Concrete.

Montemor, M. F., A. M. P. Simoes and M. G. S. Ferreira (1998). "Analytical characterization of the passive film formed on steel in solutions simulating the concrete interstitial electrolyte." Corrosion 54(5): 347-353.

Muste, M., Z. Xiong, J. Schone and Z. Li (2004). "Validation and Extension of Image Velocimetry Capabilities for Flow Diagnostics in Hydraulic Modeling." Hydraulic Engineering 130(3): 175-185.

Nagano, H. and T. Naito (1985). "Application of diffusion theory to chloride penetration into concrete located in splashing zones." Transactions of the Japan Concrete Institute 7: 157-164.

Ollivier, J. P., J. C. Maso and B. Bourdette (1995). "Interfacial Transition Zone in Concrete." Advanced Cement Based Material 2(1): 30-38.

Ost, B. and G. E. Monfore (1966). "Penetration of chloride into concrete." Journal of the P.C.A. Research and Development Laboratories.

Otsuki, N., S. Sagataki and K. Nakashita (1992). " Evaluation of AgN03 solution spray method for measurement of chloride penetration into hardened cementitious matrix materials." ACI Materials Journal 89(6): 587-592.

Page, C. L., N. R. Short and A. Tarras (1981). "Diffusion of Chloride Ions in Hardened Cement Pastes." CEMENT and CONCRETE RESEARCH 11(3): 395-406.

Pérez, B. M., S. J. Pantazopoulou and M. D. A. Thomas (2001). "Numerical solution of mass transport equations in concrete structures." computers and structures 79(13): 1251-1264.

Pérez, B. M., H. Zibara, R. D. Hooton and M. D. A. Thomas (2000). "A study of the effect of chloride binding on service life predictions." CEMENT and CONCRETE RESEARCH 30(8): 1215-1223.

Ping, X., J. J. Beaudoin and R. Brousseau (1991). "Flat aggregate-portland cement paste interfaces, I. electrical conductivity models." CEMENT and CONCRETE RESEARCH 21(4): 515-522.

Poinard, C., E. Piotrowska, Y. Malecot, L. Daudeville and E. N. Landis (2012). "Compression triaxial behavior of concrete: the role of the mesostructure by analysis of X-ray tomographic images." European Journal of Environmental and Civil Engineering 16(1): 115-136.

Pourbaix, M. (1974). "Atlas of Electrochemical Equilibria in Aqueous Solutions." Houston, Tex., National Association of Corrosion Engineers.

Princeton Applied Research (2005). Electrochemistry and corrosion overview and techniques, Application Note corr-4, http://new.ametek.com/content-manager/files/PAR/088.pdf.

Rangaraju, P. R., J. Olek and S. Diamond (2010). "An investigation into the influence of inter-aggregate spacing and the extent of the ITZ on properties of Portland cement concretes." CEMENT and CONCRETE RESEARCH 40(11): 1601-1608.

Rangayyan, R. M. (2005). "The Biomedical Image Analysis." CRC Press LLC.

Ritter, N. and J. Cooper (2009). "New Resolution Independent Measures of Circularity." Mathematical Imaging and Vision 35(2): 117-127.

Russ, J. C. (2011). "The image processing handbook." Boca Raton, Taylor & Francis.

Scrivener, K. L., A. K. Crumbie and P. Laugesen (2004). "The Interfacial Transition Zone (ITZ) Between Cement Paste and Aggregate in Concrete." Interface Science 12(4): 411-421.

Scrivener, K. L. and P. L. Pratt (1986). "A preliminary study of the microstructure of the cement paste-aggregate bond in mortars." 8th International Congress on the Chemistry of Cement, Rio de Janeiro.

Scrivener, K. L. and P. L. Pratt (1996). "Characterization of interfacial microstructure." Interfacial Transition Zone in Concrete. London, E & N Spon.

Shih, F. (2009). Image processing and mathematical morphology fundamentals and applications.

Shin, C. B. and E. K. Kim (2002). "Modeling of chloride ion ingress in coastal concrete." CEMENT and CONCRETE RESEARCH 32(5): 757-762.

Silverman, D. C. "Tutorial on POLEXPERT and the cyclic potentiodynamic polarization technique." http://www.argentumsolutions.com:80/tutorials/polexpert_tutorialpg1.html, Argentum Solutions, Inc.

Stern, M. and A. L. Geary (1957). "Electrochemical polarisation: I. A theoretical analysis of the shape of polarisation curves." Journal of The Electrochemical Society 104(1): 56-63.

Stratfull, R. F. (1968). "Laboratory corrosion test of steel in concrete." Sacramento, California, California division of highways, State of California.

Stratfull, R. F. (1972). "Half-cell potential and the corrosion of steel in concrete." Sacramento, California, California division of highways, State of California.

Sun, H. Q. and Y. Luo (2009). "Adaptive watershed segmentation of binary particle image." Microscopy 233(2): 326-330.

Suwito, A. and Y. Xi (2006). "Parallel finite element method for coupled chloride moisture diffusion in concrete." International Journal of Numerical Analysis and Modeling 3(4): 481-503.

Thuresson, T. I. (1996). "Electrochemical monitoring of the influence of concrete quality on the reinforcing steel corrosion in industrial effluent." Queen's University. MA. Sc. .

Uhlig, H. H. (1967). "Structure and growth of thin films on metals exposed to oxygen." Corrosion Science 7: 325-339.

Weyers, R. E. and D. G. Smith (1989). "Chloride Diffusion Constant for Concretes." Structural Materials ASCE: 106-115.

Wonga, H. S., Y. X. Zhaob, A. R. Karimia, N. R. Buenfelda and W. L. Jinb (2010). "On the penetration of corrosion products from reinforcing steel into concrete due to chloride-induced corrosion." Corrosion Science 52(7): 2469-2480.

Xi, Y. and Z. P. Bažant (1999). "Modeling chloride penetration in saturated concrete." Journal of Materials in Civil Engineering 11(1): 58-65.

Xiao, J., J. Ying and L. Shen (2012). "FEM simulation of chloride diffusion in modeled recycled aggregate concrete." Construction and Building Materials 29: 12-23.

Yuan, Q., C. Shi, G. D. Schutter, K. Audenaert and D. Deng (2009). "Chloride binding of cement-based materials subjected to external chloride environment – A review." Construction and Building Materials 23(1): 1-13.

Zakroczymski, T., C.-J. Fan and Z. Szklarska-Smialowska (1985). "Kinetics and mechanism of passive film formation on iron in 0.05M NaOH." Journal of Electrochemical Society 132(12): 2862-2867.

Zakroczymski, T., C.-J. Fan and Z. Szklarska-Smialowska (1985). "Passive film formation on iron and film breakdown in a sodium hydroxide solution containing chloride ions." Journal of Electrochemical Society 132(12): 2868-2871.

Zeng, Y. (2007). "Modeling of chloride diffusion in hetero-structured concretes by finite element method." Cement and Concrete Composites 29(7): 559-565.

Zheng, J. and X. Zhou (2008). "Three-Phase Composite Sphere Model for the Prediction of Chloride Diffusivity of Concrete." Materials in Civil Engineering 20(3): 205-211.

Zheng, J. J., C. Q. Li and X. Z. Zhou (2005). "Characterization of Microstructure of Interfacial Transition Zone in Concrete." Materials Journal 102(4): 265-271.

Ziou, D. and S. Tabbone (1998). "Edge detection techniques- an overview." Pattern recognition and image analysis 8(4): 537-559.